




Article

Pb(II) Removal from Aqueous Solutions by Adsorption on Stabilized Zero-Valent Iron Nanoparticles—A Green Approach

Saloome Sepehri ^{1,*}, Elahe Kanani ², Sima Abdoli ³ , Vishnu D. Rajput ⁴ , Tatiana Minkina ⁴ 
and Behnam Asgari Lajayer ^{5,*}

¹ Agricultural Engineering Research Institute (AERI), Agricultural Research, Education and Extension Organization (AREEO), Karaj P.O. Box 31585-845, Iran

² Department of Water Sciences and Engineering, Imam Khomeini International University, Qazvin P.O. Box 3414896818, Iran

³ Department of Soil Science and Engineering, Shahid Chamran University of Ahvaz, Ahvaz 6135743136, Iran

⁴ Academy of Biology and Biotechnology, Southern Federal University, 344090 Rostov-on-Don, Russia

⁵ Department of Soil Science, Faculty of Agriculture, University of Tabriz, Tabriz 5166616422, Iran

* Correspondence: sepehri_saloome@yahoo.com (S.S.); h-asgari@tabrizu.ac.ir (B.A.L.)

Abstract: Nano zero-valent iron particles (nZVFe) are known as one of the most effective materials for the treatment of contaminated water. However, a strong tendency to agglomerate has been reported as one of their major drawbacks. The present study describes a green approach to synthesizing stabilized nZVFe, using biomass as a porous support material. Therefore, in the first step, biomass-derived activated carbon was prepared by thermochemical procedure from rice straw (RSAC), and then the RSAC-supported nZVFe composite (nZVFe–RSAC) was employed to extract Pb(II) from aqueous solution and was successfully synthesized by the sodium borohydride reduction method. It was confirmed through scanning electron microscopy (SEM) and X-ray diffraction (XRD) characteristics that the nZVFe particles are uniformly dispersed. Results of the batch experiments showed that 6 (g L⁻¹) of this nanocomposite could effectively remove about 97% of Pb(II) ions at pH = 6 from aqueous solution. The maximum adsorption capacities of the RS, RSAC, and nZVFe–RSAC were 23.3, 67.8, and 140.8 (mg g⁻¹), respectively. Based on the results of the adsorption isotherm studies, the adsorption of Pb(II) on nZVFe–RSAC is consistent with the Langmuir–Freundlich isotherm model ($R^2 = 0.996$). The thermodynamic outcomes exhibited the endothermic, possible, and spontaneous nature of adsorption. Adsorption enthalpy and entropy values were determined as 32.2 kJ mol⁻¹ and 216.9 J mol⁻¹ K⁻¹, respectively. Adsorption kinetics data showed that Pb(II) adsorption onto nZVFe–RSAC was fitted well according to a pseudo-second-order model. Most importantly, the investigation of the adsorption mechanism showed that nZVFe particles are involved in the removal of Pb(II) ions through two main processes, namely Pb adsorption on the surface of nZVFe particles and direct role in the redox reaction. Subsequently, all intermediates produced through the redox reaction between nZVFe and Pb(II) were adsorbed on the nZVFe–RSAC surface. According to the results of the nZVFe–RSAC recyclability experiments, even after five cycles of recovery, this nanocomposite can retain more than 60% of its initial removal efficiency. So, the nZVFe–RSAC nanocomposite could be a promising material for permeable reactive barriers given its potential for removing Pb(II) ions. Due to low-cost and wide availability of iron salts as well as rice biowaste, combined with the high adsorption capacity, make nZVFe–RSAC an appropriate choice for use in the field of Pb(II) removal from contaminated water.

Keywords: adsorption capacity; biomass-derived activated carbon; lead; nanocomposite; redox reaction; zero-valent iron nanoparticles



Citation: Sepehri, S.; Kanani, E.; Abdoli, S.; Rajput, V.D.; Minkina, T.; Asgari Lajayer, B. Pb(II) Removal from Aqueous Solutions by Adsorption on Stabilized Zero-Valent Iron Nanoparticles—A Green Approach. *Water* **2023**, *15*, 222. <https://doi.org/10.3390/w15020222>

Academic Editor: Laura Bulgariu

Received: 29 November 2022

Revised: 28 December 2022

Accepted: 30 December 2022

Published: 4 January 2023



Copyright: © 2023 by the authors. Licensee MDPI, Basel, Switzerland. This article is an open access article distributed under the terms and conditions of the Creative Commons Attribution (CC BY) license (<https://creativecommons.org/licenses/by/4.0/>).

1. Introduction

Heavy metals (HMs) have become a serious problem over the past few decades due to their high toxicity [1,2], ability to accumulate within the food chain, and biomagnification

characteristics [3,4]. It is important to note that many of these HMs are highly toxic, even at trace levels, resulting in widespread ecosystem damage [5–7]. One such HM is lead (Pb(II)). In such a way, water pollution caused by Pb has attracted global attention. Although Pb(II) was usually released into the environment through natural processes in the past, today HMs pollution is mainly caused by anthropogenic activities [8]. Studies have shown that damage to the kidneys, brain, nervous system, and liver is caused by the long-term use of Pb-contaminated water [9]. HM ions can be removed from contaminated water by using various methods, including chemical precipitation, reverse osmosis, hydrolysis, ion exchange, surface adsorption, and electrochemical purification [10–12].

In recent years, nanoscale zero-valent iron particles (nZVFe) with sizes ranging from 1 to 100 nm at least one dimension have shown good potential as an environmentally friendly strong reducing agent for removing various pollutant [13], for instance, HMs such as nickel (Ni), cadmium (Cd), copper (Cu), hexavalent chromium [Cr(VI)], cobalt (Co), arsenic (As), mercury (Hg), and lead (Pb) from wastewater and polluted water [14–16]. As a result of their high surface energy, direct interparticle interactions, and intrinsic magnetic interaction, bare iron nanoparticles (NPs) tend to agglomerate into micron or larger solid particles. Consequently, using bare nZVFe particles can have drawbacks, including aggregate formation, reducing specific surface area, producing a lower negative redox potential, and leading to poor mechanical and structural durability [5]. Moreover, separating ZVFe NPs from contaminated soil or treated aqueous systems is very difficult [17]. As a means of overcoming these disadvantages, the idea of immobilizing the ZVFe NPs into porous host materials was proposed and discussed in several research studies. Three main categories of porous host materials are available for the stabilization of iron NPs: (i) natural minerals, namely pillared clay [18], pumice granular [19,20], acid activated sepiolites [21,22], montmorillonite [23,24], kaolin [25], bentonite [26,27], zeolite [28–30], biochar [31,32], and charcoal [33]; (ii) biomaterials such as pine cone [34], aquatic plant *Azolla filiculoides* [35], cellulose nanofibrils [36], walnut shell [37], and macroporous alginate ([38,39]); and (iii) synthetic materials such as cationic resin [40], anion exchange resin [41], porous carbon sheet [42], chelating resin [43], titanate nanotube [44], meso-porous silica carbon [45], layered double hydroxide [46,47], activated carbon [34,48,49], graphene oxide [45,50], chitosan [51], carbon nanotube [52], magnesium (hydr)oxide [19,53], and humic acid [54].

In addition, it is possible to synthesize activated carbon by using various activating agents, and it is widely used in a variety of fields, including wastewater treatment [55–57]. From previous studies, it was found that activated carbon materials are successful adsorbents for HMs. Because of their high pore volume, they have a significant potential to trap target HM ions [58,59]. As a result of its large specific surface area, stable microporous structure, wide availability, affordability, great adsorption capacity, and compatibility with the environment, biomass-derived activated carbon (BAC) can be an appropriate support material for nZVFe particles. Consequently, in addition to stabilizing iron NPs by providing more interaction between NPs and Pb ions, it will increase the absorption capacity of the resulting composite [60,61]. On the other hand, rice is the primary crop and staple food for more than half of the world's population. According to the recent work [62], rice is the world's third most produced agricultural product, with 970 million tons produced globally in 2020. According to FAO statistics [62], the area under rice cultivation in Iran was about 4200 km², and rice cultivation is a common occupation in Iran, especially in the north, where 2 million tons are produced annually. After harvesting this large amount of rice in the fields, many biowastes, such as rice husks and straw, remain, which can be considered valuable resources for a variety of purposes. In order to fully appreciate this fact, it is important to realize that the production of each kilogram of milled rice is accompanied by the production of approximately 1100 and 280 g of rice straw and rice husk, respectively [63].

In this study, with the aim of win-win cooperation, BAC and ZVFe NPs were used together in order to verify the constructive interaction between the two counterparts and improve their remediation capability. The stabilization of nanosized iron particles on porous

BAC support occurs through different mechanisms, including coordinating, adsorption, chelating, bridging processes, and immobilizing [61]. As a result of the bidentate complexation, ferrous and ferric iron ions are complexed with -OH [64], and stable bonds are also created through the reaction between the BAC surface functionalities and the iron oxide layer formed around the nZVFe core [65]. As a result of the reduced intraparticle attraction, this phenomenon results in a reduction in ZVFe NPs' agglomeration and enhances their dispersion on the surface of the BAC support [61].

Therefore, the aims of this research were (i) the synthesis of RSAC and nZVFe-RSAC and investigation of the effects of Fe loading quantity on the properties of nanocomposite; (ii) the characterization of the novel nanocomposite with powder X-ray diffraction (XRD), Scanning Electron Microscopy (SEM), and Brunauer-Emmett-Teller (BET-N₂) technologies; (iii) to perform batch adsorption experiments under various operating conditions to determine the removal efficiency of Pb(II), investigating the effect of competing ions on the absorption of the target pollutant [Pb(II)], as well as examining nZVFe-RSAC's recyclability; and (iv) to perform a detailed study of adsorption isotherms, kinetics, and thermodynamic functions of the adsorption process. In a broad way, this research focused on synthesizing and evaluating a novel super-porous, highly efficient adsorbent from agricultural wastes which are abundant and environmentally friendly, with a high potency of toxic Pb removal.

2. Materials and Methods

2.1. Chemicals and Analytical Techniques

All chemicals used in this research were purchased from Merck or Sigma-Aldrich at analytical grade, and all preparations were carried out by using distilled water (DI). Lead (II) stock solution was prepared by using appropriate amounts of Pb(NO₃)₂ and using deionized water. The stock solution was diluted with deionized water in order to prepare solutions at different concentrations. The pH of the solutions was adjusted by using 0.1 M HNO₃ and 0.1 M NaOH solutions and controlled by a pH meter (Metrohm, 827 pH Lab). Atomic absorption spectrophotometry was used to determine the concentration of Pb(II) solutions (Perkin-Elmer 3030). Additionally, rice straw (RS) elemental analyses were conducted by using a Costech ECS 4010 Elemental Analyzer, and the physical properties and compositions of RS and RSAC were determined based on the published literature [63]. Using the standard test method, the total ash content of RS and RSAC was measured (ASTM D2866-2011). Moreover, the specific surface areas (SSAs) of the RS, RSAC, and nZVFe-RSAC samples were determined by means of a Belsorp mini II (BelJapan) instrument in accordance with the BET-N₂ method. A Barrett-Joyner-Halenda (BJH) and density functional theory (DFT) model were used to calculate the pore size and distribution of the pores, respectively [66]. A Philips X'PERTMPD diffractometer equipped with a graphite-monochromatized (Cu-K α radiation, $\lambda = 1.54 \text{ \AA}$) was employed in order to determine the XRD patterns of RS, RSAC, and nZVFe-RSAC samples. A scanning rate of $0.05 \text{ (}^\circ \text{ s}^{-1}\text{)}$ was used to record all samples between 10 and 70° (2 θ). Finally, the morphology of RS, RSAC, and nZVFe-RSAC samples was examined by SEM (Hitachi S-4160, 20.0 kV). The pH_{pzc} (point of zero charge) was measured with a zeta-meter system 3.0+ (Meditop Co., Bangkok, Thailand).

2.2. Preparation of RSAC and nZVFe-RSAC

Rice straw (RS) was collected from the local farms of Guilan province, Iran; ground; and then sieved, using a 200-mesh sieve. Thereafter, to remove ash and water-soluble substances, the samples were soaked in a solution of NaOH (2 wt.%) for 48 h. A series of washes with DI water was conducted until neutrality was reached, and then the rice straws were dried at 80 °C for 24 h and stored for later use. From the treated RS, powdered activated carbon was prepared by using a thermochemical method. As a first step toward chemical activation, the dried RS samples were pre-oxidized at 200 °C in air atmosphere for 2 h. Then the prepared samples were impregnated with a 30 wt.% (NH₄)₂ HPO₄ solution, using an impregnation mass ratio of 5(NH₄)₂ HPO₄/1 RS. Two phases of thermal treatment

were conducted on acid-impregnated samples in an electrical heating furnace, under an inert nitrogen atmosphere at a flow rate of 25 mL min^{-1} . During the first phase, a constant rate of $6 \text{ }^\circ\text{C per minute}$ was used to heat the reactor to $170 \text{ }^\circ\text{C}$, and a 60-min period was spent maintaining samples at this temperature. It was followed by heating the reactor to $500 \text{ }^\circ\text{C}$ at a rate of $8 \text{ }^\circ\text{C per minute}$ and maintaining the samples at this temperature for 60 min. After carbonization, for the purpose of preventing reoxidation of the obtained solids, the furnace was gradually cooled in a stream of nitrogen gas during the night, until it reached room temperature [67]. Following this, a solution of $1 \text{ mol L}^{-1} \text{ HCl}$ was used for washing, and a vacuum flask was used for filtering. In the following stages, hot DI water was used for repeated washing of the final product until a pH value of 7 was reached in the rinsing water. As a final step, RSAC samples were dried at $105 \text{ }^\circ\text{C}$ in a vacuum for 24 h before being stored in a desiccator. In order to synthesize nZVFe–RSAC, ferrous iron solutions were reduced by using borohydride, and RSAC served as a porous support medium. First of all, to prepare the ferrous solution, $\text{FeSO}_4 \cdot 7\text{H}_2\text{O}$ (iron/RSAC mass ratio 1:1) was dissolved in a mixture of absolute ethanol/DI water with a ratio of $1/4 (v/v)$. In the next step, the prepared solution was poured into an open flask with three necks, and the solution was stirred for four hours with 1 g of RSAC added to it. Then, on a magnetic stirrer, 55 mL of freshly prepared NaBH_4 aqueous solution ($\text{BH}_4^-/\text{Fe}^{2+}$ molar ratio of 3.0) was added to the mixture, drop by drop, leading to Fe^0 NPs formation and H_2 evolution. Subsequently, by using NaBH_4 as a reduction agent and RSAC as a porous stabilizer, nZVFe–RSAC was synthesized in the solution by reducing Fe (II) to Fe^0 . To prevent nZVFe–RSAC oxidation, N_2 was used as an inert gas throughout the entire process described. After filtering the suspension and washing it with pure ethanol three times, the synthesized nanocomposite was extracted. Following vacuum drying at $75 \text{ }^\circ\text{C}$ overnight, the nanocomposite was stored in an N_2 atmosphere for later use [68].

2.3. Procedures for Adsorption Experiments

To obtain maximum performance, the factors that affect the adsorption process, including contact time, temperature, pH, amount of adsorbent, and initial concentration of target pollutant, need to be optimized. Using deionized distilled water, appropriate amounts of $\text{Pb}(\text{NO}_3)_2$ were dissolved in order to prepare aqueous solutions of Pb(II). Firstly, the pH was optimized in the range of pH 2–10. Afterward, the removal efficiency of Pb(II) ions was investigated for different adsorbent dosages between 2 and $10 \text{ (g L}^{-1}\text{)}$. The contact time has a substantial effect on the adsorption process. In order to determine the equilibrium time of the adsorption and the best-fitted kinetic model, kinetic studies were conducted. The contact time was optimized in the range of 2–1440 min for $100 \text{ (mg L}^{-1}\text{)}$ of target pollutant. Furthermore, to study the effect of the initial lead concentration on the adsorption efficiency, equilibrium isotherm experiments were conducted by using different initial lead concentrations ranging from 10 to $1000 \text{ (mg L}^{-1}\text{)}$. During these experiments, the initial pH of the solutions and the initial adsorption temperature were fixed at the (6 ± 0.1) and $(25 \pm 1 \text{ }^\circ\text{C})$, respectively. Finally, the temperature effect on the Pb(II) removal efficiency was investigated in the range of $25\text{--}50 \text{ }^\circ\text{C}$.

The batch experiments were conducted by using 0.1 g of sorbent and 10 mL of lead solution, at the desired pH and concentration, in polyethylene bottles (50 mL). Mixing was performed with a shaker at 200 rpm. In every batch adsorption experiment, three replicates of each type and concentration of water solution were produced to ensure representative results. A series of samples was collected throughout the adsorption experiments, filtered, and the target pollutant concentration was determined in the supernatant immediately after filtering. By using Equations (1) and (2), the adsorption capacity of sorbents ($q_e \text{ (mg g}^{-1}\text{)}$) and the removal efficiency Pb(II) ($\text{Re } \%$) were determined:

$$q_e = \frac{(C_0 - C_e) \times V}{W} \quad (1)$$

$$\text{Re}(\%) = \frac{C_0 - C_e}{C_0} \times 100 \quad (2)$$

where C_0 (mg L^{-1}) is the initial concentration of the target pollutant, and C_e (mg L^{-1}) represents the equilibrium concentration of the target pollutant. The V (L) and W (g) are the volume of adsorbate solution and the mass of adsorbent, respectively.

An evaluation of the effects of Fe loading quantities on the adsorption capacity of Pb(II) was conducted in order to optimize the preparation process for the nZVFe–RSAC nanocomposite. For this purpose, different nanocomposites were prepared with different mass ratios of Fe:RSAC, including 0:1, 0.2:1, 0.5:1, 1:1, 2:1, and 5:1. A similar mass of these adsorbents was then subjected to solutions containing 100 mg L^{-1} of Pb(II) in order to determine their adsorption capacities for Pb(II). The nanocomposite with the highest Pb(II) adsorption capacity was selected for further batch studies in regard to characterization, pH effect, adsorbents dosage, competing ions, and adsorption kinetics, isotherms, and thermodynamics.

To evaluate the effect of competing ions on the Pb(II)-removal efficiency, 0.5 g of adsorbent was added to solutions containing 30 mg L^{-1} Pb(II) and varying concentrations of background competitors ($50\text{--}200 \text{ mg L}^{-1}$), including Ni (II), Hg (II), Cu (II), and Cd (II), while maintaining the solution pH level at 6.0 ± 0.5 . The solution of competing ions was prepared by using Hg Cl_2 , $\text{Ni (NO}_3)_2$, and $\text{Cu (NO}_3)_2$ salts.

In addition, nZVFe–RSAC's recyclability and reusability were evaluated through repeated cycles of Pb(II) adsorption and desorption at an initial concentration of 50 mg L^{-1} for six consecutive cycles. Following the first cycle, the used nanocomposite was regenerated by washing it in HCl, (0.01 M) for removing the oxide layer and dissolving the precipitated. In the following step, the nanocomposite was washed with DI water, dried under vacuum overnight, and stored for the next treatment cycle [17]. Three parallel measurements were used to determine the average value of Pb(II) removal efficiency, using Equation (2).

2.4. Adsorption Kinetics, Isotherms, and Thermodynamics

In the present study, four widely used isotherm models, namely Redlich–Peterson (Equation (3)), Langmuir (Equation (4)), Langmuir–Freundlich (Equation (5)), and Freundlich (Equation (6)) [69,70] were employed to describe the isothermal behavior of adsorption. Modeling the experimental target pollutant (Pb(II)) isotherm data is required to understand the adsorption behavior and removability of adsorbents.

$$q_e = \frac{aC_e}{1 + bC_e^g} \quad (3)$$

$$q_e = \frac{q_m k_L C_e}{1 + k_L C_e} \quad (4)$$

$$q_e = \frac{q_m k_{LF} C_e^{\frac{1}{n}}}{1 + k_{LF} C_e^{\frac{1}{n}}} \quad (5)$$

$$q_e = k_F C_e^{\frac{1}{n}} \quad (6)$$

where the q_e (mg g^{-1}) refers to the amount of adsorbed ions per unit mass of adsorbent at equilibrium condition; C_e (mg L^{-1}) refers to the equilibrium concentration of ions in the solution; q_m (mg g^{-1}) represents the maximum sorption capacity of the used adsorbent for target pollutant; and k_L (L mg^{-1}), n , a , b , k_{LF} (L mg^{-1}), and k_F (mg g^{-1}) are constants, and g in an exponent.

Furthermore, the kinetic models can help us understand the rate and order of the adsorption process and, therefore, to evaluate the performance of adsorbents. So, in this research, the experimental data were fitted to a number of kinetic models, such as pseudo

second-order (Equation (7)), Elovich (Equation (8)), intraparticle diffusion (Equation (9)), and pseudo-first-order (Equation (10)) models [71].

$$q_t = \frac{k_2 q_e^2 t}{1 + k_2 q_e t} \quad (7)$$

$$q_t = \frac{1}{\beta} \ln(\alpha\beta) + \frac{1}{\beta} \ln(t) \quad (8)$$

$$q_t = k_p t^{0.5} + C_p \quad (9)$$

$$q_t = q_e (1 - e^{-k_1 t}) \quad (10)$$

where q_t and q_e (mg g^{-1}) represent the quantity of the target pollutant sorbed by adsorbent at time t (min) and equilibrium condition, respectively; k_1 (min^{-1}) and k_2 ($\text{g mg}^{-1} \text{min}^{-1}$) are the pseudo-first-order and pseudo-second-order kinetic models' rate constants, respectively; k_p ($\text{mg g}^{-1} \text{min}^{-0.5}$) demonstrates the rate constant of the intraparticle diffusion; and a constant C_p (mg g^{-1}) represents the thickness of the boundary layer of sorbent-sorbate system. Furthermore, α ($\text{mg g}^{-1} \text{min}^{-1}$) and β (g mg^{-1}) represent the adsorption rate at the start and the adsorption constant, respectively.

It is possible to calculate h ($\text{mg g}^{-1} \text{min}^{-1}$), the initial absorption rate, as follows:

$$h = k_2 q_e^2 \quad (11)$$

The models' parameters (Equations (3)–(10)) were evaluated and best utilized by nonlinear regression, which was performed by using the GraphPad Prism (V.7) tool. Among the applied models, the best fitted for the experimental data was evaluated based on the results of the determination coefficient (R^2), in addition to Standard Error of Estimate (SEE). These two statistical parameters were calculated based on the comparison of the experimental and calculated values.

The adsorption behavior and spontaneity of adsorption processes are largely determined by thermodynamic studies. Further details are provided regarding the appropriate temperature range for the adsorption process, as well as the nature of the adsorbent and sorbate under equilibrium conditions. In order to accomplish this goal, using Equations ((12)–(14)), thermodynamic factors such as free energy (ΔG^0), enthalpy (ΔH^0), and entropy (ΔS^0) were calculated [72]:

$$\Delta G^0 = -RT \ln k_d \quad (12)$$

$$\ln k_d = \frac{\Delta S^0}{R} - \frac{\Delta H^0}{RT} \quad (13)$$

$$k_d = \frac{q_e}{C_e} \quad (14)$$

where $[\Delta G^0$ (kJ mol^{-1})], $[\Delta S^0$ ($\text{J mol}^{-1} \text{K}^{-1}$)], and $[\Delta H^0$ (kJ mol^{-1})] represent variations in Gibbs free energy, entropy, and enthalpy, respectively; R ($8.314 \text{ J mol}^{-1} \text{K}^{-1}$) and T ($^{\circ}\text{K}$) are the gas constant and temperature, respectively; k_d is the thermodynamic equilibrium constant; q_e (mg L^{-1}) is the solid phase equilibrium concentration; and C_e (mg L^{-1}) represents the solution equilibrium concentration.

3. Results and Discussion

3.1. Characterization of RS, RSAC, and nZVFe–RSAC Composite

The elemental analysis and structural components of RS are summarized in Table 1, and the physicochemical characteristics of RSAC are demonstrated in Table 2.

Table 1. Characteristics of the RS sample.

Structural Components (%)					Elemental Analysis (wt.%)			
Cellulose	Hemicelluloses	Lignin	Extractives	Ash	Carbon	Oxygen	Hydrogen	Nitrogen
39.25	29.18	25.42	5.89	2.83	39.65	45.63	8.21	3.14

Table 2. Physicochemical characteristics of the RSAC sample.

Bulk Density (kg m ⁻³)	Iodine Number (mg g ⁻¹)	Elemental Analysis (wt.%)				
		Ash	Carbon	Oxygen	Hydrogen	Nitrogen
470	830	3.53	80.77	9.10	3.02	3.54

Additionally, Table 3 displays the BET surface areas (S_{BET} (m² g⁻¹)), total specific pore volumes (V_{T} cm⁻¹ g⁻¹), and specific micropore volumes (V_{M} cm⁻¹ g⁻¹) of the RS, RSAC, and nZVFe–RSAC adsorbents. RS, RSAC, and nZVFe–RSAC adsorbents have BET surface areas of 5.14, 406.87, and 697.19 (m² g⁻¹), respectively. The immobilization of the nZVFe particles onto RSAC leads to an increase in the BET surface area, as well as the pore volume of the nZVFe–RSAC.

Table 3. Textural characterization of the RS, RSAC, and nZVFe–RSAC samples.

Sample	Pore Volume (cm ³ g ⁻¹)			Mean Pore Width (nm)
	S_{BET} (m ² g ⁻¹)	V_{T} (cm ⁻¹ g ⁻¹)	V_{M} (cm ⁻¹ g ⁻¹)	
RS	5.14	0.024	-	-
RSAC	406.87	0.384	0.062	2.7
nZVFe–RSAC	697.19	0.641	0.094	1.8

As mentioned earlier, the morphologies of RS, RSAC, and nZVFe–RSAC were analyzed by using SEM (Figure 1a–c). From the SEM micrograph of RS (Figure 1a), low porosity and a rough and uneven texture of the external surface were detected. This is consistent with the findings of the research [66]. The SEM image of the adsorbent after carbonization (Figure 1b) clearly illustrates its super-porous surface, which is indicative of a relatively high surface area [69]. Upon immobilization of nZVFe particles onto the RSAC surface, the morphology of the nZVFe–RSAC changed. A uniform distribution of these particles of a core–shell structure was observed on the surface of the stabilizer. SEM images were reviewed, and 100 particles' diameters were measured in different regions to determine the size of stabilized nZVFe particles. Based on this method, in the case of nZVFe–RSAC, the nZVFe particle ranged in size from 30 to 65 nm, corresponding to a mean particle diameter of 46 nm, without any apparent aggregation. The RSAC surface was strongly adsorbing Fe(II) ions, which generally occupied channel spaces. Using NaBH₄, these ions were then reduced to Fe⁰. Subsequently, nZVFe particles were dispersed uniformly on the RSAC, forming a super-porous nanocomposite. The SSAs of RSAC and nZVFe–RSAC also support this statement. As previously reported (Table 4), the SSA of nZVFe–RSAC was 1.7 times higher than the SSA of the RSAC. Similar results were obtained by using chitosan and bentonite-supported iron nanoparticles for removing Cr(VI) from aqueous solutions [25,51].

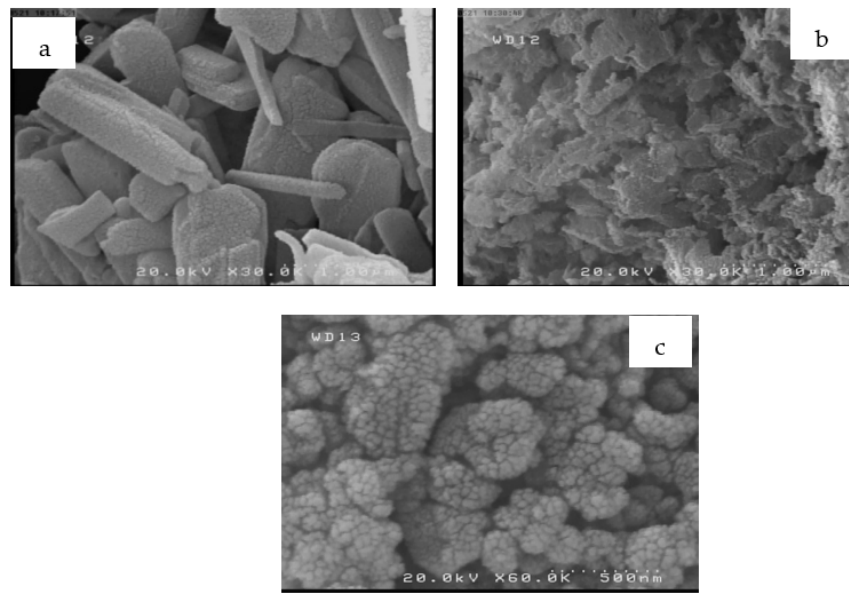


Figure 1. SEM images of: (a) RS, (b) RSAC, and (c) nZVFe-RSAC.

Table 4. The kinetic parameters of the adsorption of Pb(II) on the RS, RSAC, and nZVFe-RSAC.

Model	Parameters	Adsorbent		
		RS	RSAC	nZVFe-RSAC
Pseudo-first order	q_e (mg g ⁻¹) (Exp)	16.67	20.93	24.24
	q_e (mg g ⁻¹) (Cal)	18.21	20.78	23.28
	k_1 (min ⁻¹)	0.008	0.012	0.091
	R^2	0.982	0.916	0.604
	SEE	0.070	0.149	0.457
Pseudo-second order	q_e (mg g ⁻¹) (Cal)	20.62	22.51	24.39
	k_2 (g mg ⁻¹ min ⁻¹)	0.0004	0.001	0.006
	h (mg g ⁻¹ min ⁻¹)	0.17	0.51	3.57
	R^2	0.968	0.964	0.896
	SEE	0.044	0.058	0.153
Intraparticle diffusion	k_p (mg g ⁻¹ min ^{-0.5})	0.467	0.435	0.203
	C_p	-4.089	-8.31	-18.73
	R^2	0.770	0.793	0.586
	SEE	0.287	0.250	0.673
Elovich	α	0.530	0.283	2.182
	β	0.265	1.75	0.552
	R^2	0.919	0.955	0.852
	SEE	0.139	0.121	0.159

Figure 2 shows the XRD patterns of RS, RSAC, and nZVFe-RSAC before and after reacting with the lead solution. The XRD pattern of RS (Figure 2a) possessed some degree of crystallinities, where the peaks at $2\theta = 27.5^\circ$, $2\theta = 22.3^\circ$, and $2\theta = 15.4^\circ$ and could be associated with the graphite structure, cellulose, and amorphous carbon in the carbonaceous material, respectively [69]. Figure 2 shows the XRD patterns of RS, RSAC, and nZVFe-RSAC before and after reacting with the lead solution. The XRD pattern of RS (Figure 2a) possessed some degree of crystallinities, where the peaks at $2\theta = 27.5^\circ$, $2\theta = 22.3^\circ$, and $2\theta = 15.4^\circ$ could be associated with the graphite structure, cellulose, and amorphous carbon in the carbonaceous material, respectively [73,74]. According to the nZVFe-RSAC XRD results (Figure 2c), the iron generally exists in zero-valent states (α -Fe) with apparent reflections at $2\theta = 44.9^\circ$ and $2\theta = 65.2^\circ$. The XRD pattern of this nanocomposite contained

no significant amount of iron oxides. Furthermore, it can be observed that nZVFe–RSAC had a typical RSAC structure, meaning that the framework of RSAC and its total crystalline structure did not change significantly after the stabilization of nZVFe particles (Figure 2c). The Scherrer equation [75] was employed to compute the particle diameter of nZVFe–RSAC. According to this equation, the nZVFe–RSAC particle diameter was about 40 nm, which corresponded well with the size determined by the SEM image (46 nm).

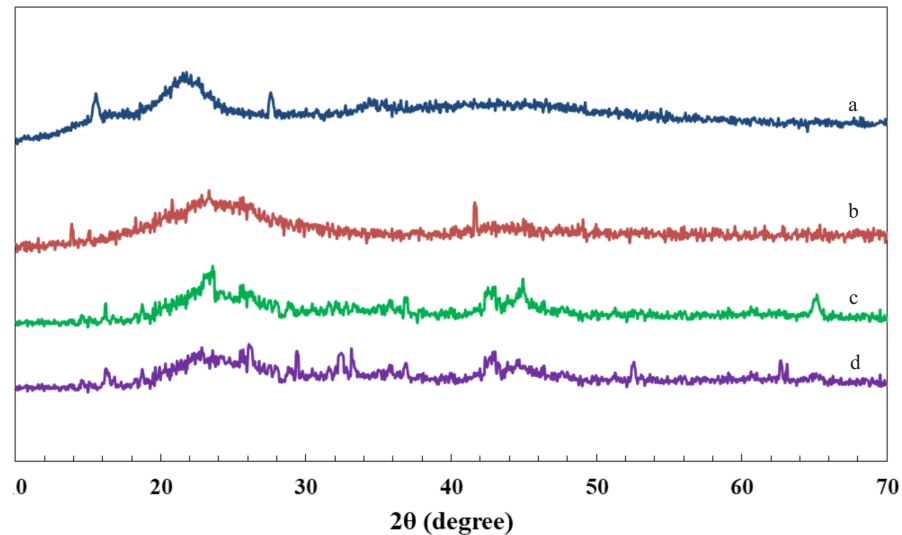
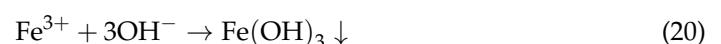
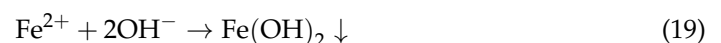
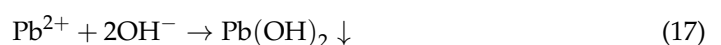
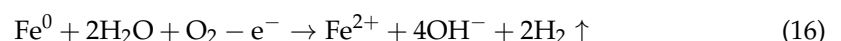
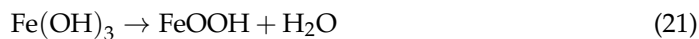


Figure 2. X-ray diffraction patterns of (a) RS, (b) RSAC, and (c) nZVFe–RSAC before reacting with Pb(II); and (d) nZVFe–RSAC(2) after reacting with Pb(II).

An examination of the XRD pattern of the nZVFe–RSAC after the reaction with the lead solution could be beneficial to interpreting the mechanism of Pb(II) removal from the aqueous solutions. After reacting with Pb(II) ions (Figure 2d), sharp peaks related to α -Fe are weakened noticeably compared with the nZVFe–RSAC XRD pattern before reacting with Pb(II). In contrast, new peaks related to iron oxide appeared in the XRD pattern of the nZVFe–RSAC (Figure 2d). As Fe^0 has strong reducing properties, it reacts with Pb^{2+} ions in the solution and consumes them. As Pb^0 and Fe^{2+} are involved in the product, Fe^{2+} will eventually undergo oxidation since it is unstable in an aerobic environment [76]. As a result, two peaks at $2\theta = 33.6^\circ$ and $2\theta = 63.0^\circ$ could be assigned to goethite (α - FeOOH) and maghemite (α - Fe_2O_3), respectively. During the removal of Pb^{2+} , phase transformation between iron phases took place. In addition, the peak corresponds to $\text{PbO}\cdot x\text{H}_2\text{O}$ at $2\theta = 29.4^\circ$, and the peaks related to $\text{Pb}(\text{OH})_2$ at $2\theta = 26.2^\circ$, $2\theta = 32.4^\circ$, and $2\theta = 33.15^\circ$ can be identified in Figure 2d. This proves the reduction of Pb^{2+} to Pb^0 . It has been found that the interaction of ZVFe nanoparticles with water leads to the formation of OH^- . In the next step, OH^- reacts with Fe^{2+} , Fe^{3+} , and Pb^{2+} in the solution, resulting in precipitates of corresponding hydroxides. Due to its instability, $\text{Fe}(\text{OH})_3$ dehydrates to Fe_2O_3 . Lead ions could eventually be able to bind to additional adsorption sites through this process [76,77]. Equations (15)–(22) could explain the mechanism of lead adsorption by nZVFe–RSAC:





The results indicate that a redox reaction occurred between ZVFe NPs and Pb(II) ions in the solution, resulting in the formation of Pb⁰ and iron oxides in the XRD pattern of the nanocomposite after its reaction with the lead solution. Subsequently, all intermediates produced through the redox reaction between iron NPs and Pb(II) were adsorbed on the nZVFe–RSAC surface and did not enter the solution. In this regard, this adsorbent is beneficial for the adsorption of lead.

3.2. Effect of Fe Loading Quantity on Nanocomposite Adsorption Capacity

In Figure 3, the effect of different Fe-loading quantities on RSAC is illustrated in terms of the specific surface areas of the nanocomposites and their adsorption capacities for Pb(II). Increasing the Fe:RSAC mass ratio from 0:1 to 1:1 resulted in a drastic increase in nanocomposite adsorption capacity for Pb²⁺, from 16.7 to 19.4 mg g⁻¹ (Figure 3). This is due to the fact that higher Fe loadings enhance nZVFe–RSAC's specific surface area. By increasing the Fe:RSAC mass ratio from 0:1 to 0.2:1 to 0.5:1 to 1:1, the S_{BET} increased from 406.9 to 433.3 to 564.7 to 697.2 m² g⁻¹. However, further increases in the Fe loading quantities from the Fe:RSAC mass ratio of 1:1 to 1:2 and 1:5 resulted in a slight decrease in the S_{BET} from 697.2 to 670.0 and 651.5, respectively. As a consequence, the Pb(II) adsorption capacity decreased from 19.4 to 19 and 18.4 mg g⁻¹. This may be explained by the relationship between the loaded Fe content (wt.%) and the adsorption process associated with the specific surface area of nanocomposite (m² g⁻¹). It is expected that the nZVFe loading on the RSAC will increase with an increase in FeSO₄ concentration, which may result in some subsequences, such as increasing the size of nanoparticles, causing the aggregation of ZVFe nanoparticles, and decreasing the uniformity of the dispersion of nZVFe particles. All of these factors may hinder the contact between the active sites and the Pb(II) ions, thereby reducing the adsorption capacity of the target pollutant. There has been similar research reported by Zhang et al. [78] and Li et al. [79]. To summarize, the best Fe:RSAC mass ratio for the preparation of nZVFe–RSAC nanocomposites was 1:1, which was used for all batch adsorption studies.

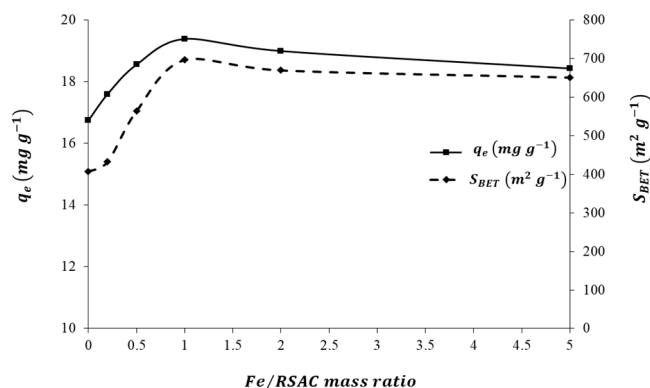


Figure 3. Effect of Fe loading quantity on nanocomposite adsorption capacity of Pb(II).

3.3. Effects of pH Value, Zeta Potential, and Absorbent Dosage on Experimental Results

The effects of the initial pH of the solution on the Pb(II) adsorption capacity and removal efficiency of different sorbents are shown in Figure 4a,b. The solution's acidity, as a major influencing factor, plays a significant role in the sorption process [80]. As indicated by the results, the pH of the solution at the beginning had a significant impact on the removal of Pb(II). Figure 4a shows that the sorption capacities of Pb(II) ions increased substantially with pH as it increased between 2.0 and 6.0 for all sorbents. A rise in pH and the activation of surface functional groups on biosorbents result in an increase in the uptake of Pb(II). The nZVFe–RSAC is observed to have a high ability to adsorb Pb(II) and

to be more sensitive to acidity in solution than other adsorbents. At pH = 6, the maximum Pb(II) removal was achieved by using the nZVFe–RSAC (Figure 4b). Other studies have reported similar findings [76,80]. After that, with a further increase in pH, the amount of lead adsorption not only did not increase but also decreased slightly. Based on the analysis, the following reasons may be responsible: (1) Several hydroxyl low-soluble species can be formed at pH values higher than 6, including $\text{Pb}(\text{OH})_2$. This leads to a decrease in lead absorption [10]. (2) Upon increasing the pH, Fe(II) and Fe(III) precipitation gradually formed, covering the shell of nZVFe particles [8], and consequently reduced the adsorption capacity of nanocomposite.

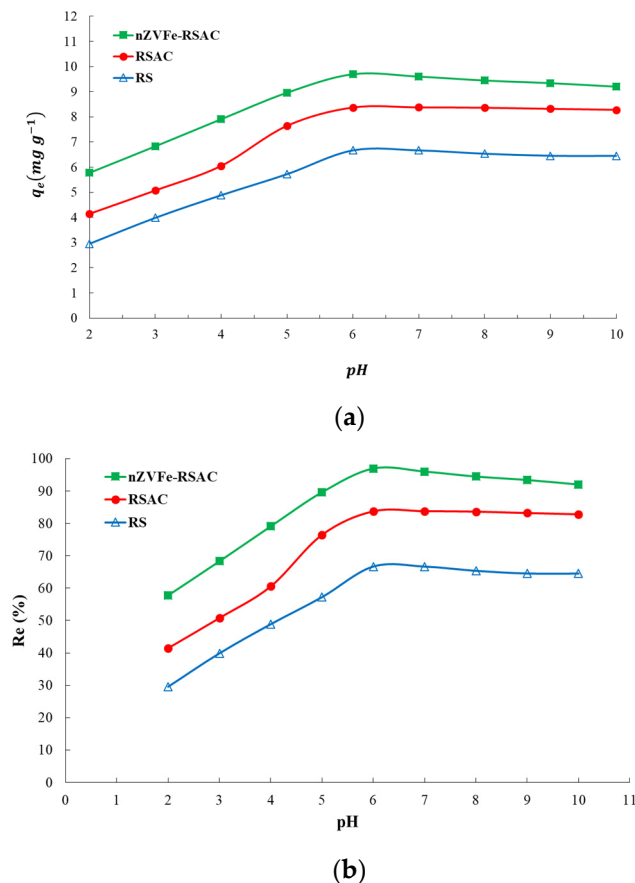


Figure 4. Pb(II) adsorption capacity (a) and removal efficiency (b) of RS, RSAC, and nZVFe–RSAC at different pH levels.

An analysis of the changes in surface charges in a 10^{-3} M KNO_3 aqueous solution was performed (Figure 5). Whenever the pH is less than pH_{pzc} (pH value of point of zero charge), the sorbent has a positive surface charge, whereas when the pH is greater than pH_{pzc} , the surface charge of the sorbent is negative. Based on Figure 5, the pH_{pzc} of the RS is approximately 6.4. After being modified by using a thermal–chemical method, the pH_{pzc} of biomass-derived activated carbon (RSAC) was shifted to 5.2. Furthermore, after stabilizing nZVFe particles on the surface of RSAC, the pH_{pzc} of the nanocomposite was also shifted to around 4, while that of pure nZVI was in the pH of range of 8–9 [81]. RSAC and nZVFe–RSAC produce acidic surfaces since their pH_{pzc} values are lower than those of unmodified RS, and this acidity may result from the generation of oxygen-containing functional groups. The reduction of Pb(II) ions is believed to be the major factor involved in the adsorption of Pb(II) ions on the nanocomposite. In addition, a role for the protonation/deprotonation of the hydroxyl species on the structure of nZVFe, as well as the precipitation of lead hydroxide, might be ascribed to the Pb(II) uptake at $\text{pH} > 4$ [82]. The literature frequently

estimates the optimum pH range for toxic metal adsorption to be between 5 and 7 [83]. In this study, a pH of 6.0 was found to be optimal for the optimum adsorption of Pb(II).

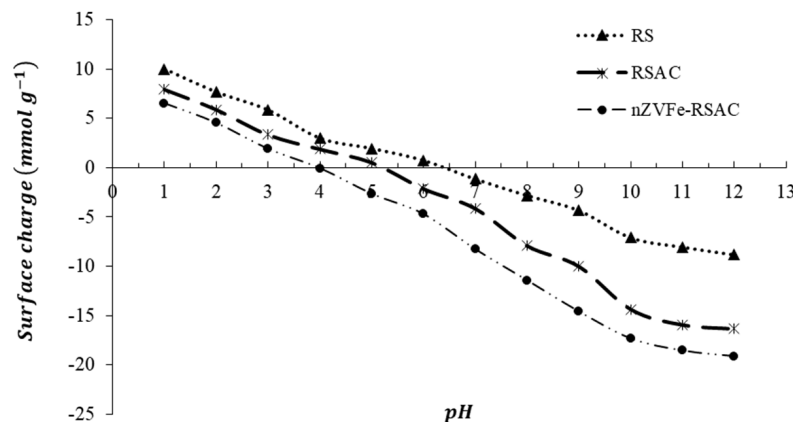


Figure 5. Zeta potential of the RS, RSAC, and nZVFe-RSAC as a function of pH.

As shown in Figure 6, different adsorbent dosages (2–10 g L⁻¹) were examined to figure out the most optimal dosage of adsorbents. These experiments were conducted with the solution’s lead concentration and pH set at 100 (mg L⁻¹) and 6, respectively. It is evident from Figure 6 that the rate of removal of Pb(II) ions increased with increasing doses of adsorbents. Increasing the nZVFe-RSAC dosage from 2 to 6 (g L⁻¹) resulted in a significant increase in the removal efficiency of Pb(II) ions from 70.1% to 96.9%. This phenomenon can be explained by the increased adsorbent surface area and the increased number of available sorption sites as a result of the increased amount of nanocomposite [8]. However, when the dosage of nZVFe-RSAC reached 8 and 10 g L⁻¹, the lead-removal percentage showed little difference, which reflected that 6 (g L⁻¹) of this nanocomposite was capable of effectively removing Pb(II) ions. There may be a connection between this phenomenon and the saturation of the active sites [84].

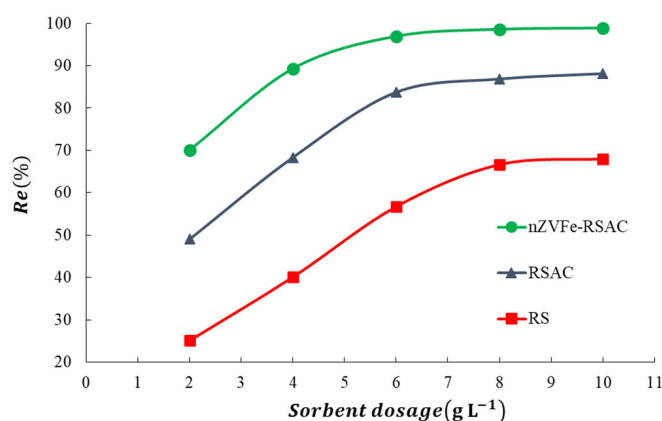


Figure 6. Effect of sorbent dosage on the Pb(II) adsorption by RS, RSAC, and nZVFe-RSAC.

3.4. Kinetic Study and Contact-Time Effects

The Pb(II)-removal efficiency was investigated with respect to exposure time to gain insight into the reaction process. For the purpose of determining the minimum time required for equilibrium adsorption, a range of time intervals was examined from 10 to 1440 min. Figure 7 displays the exposure time effects on the Pb(II) adsorption by RS, RSAC, and nZVFe-RSAC. According to Figure 7, the uptake of Pb(II) by the nanocomposite was much faster than the other adsorbents in the first 100 min and then continued with a gentle gradient up to 150 min. Then it was fixed with a slight change up to 250 min, and all Pb²⁺ and Pb(OH)⁺ cations were eliminated from the solution at working pH. One

possible explanation could be that all adsorption sites were initially unused and that there was a gradient of solute concentration across all adsorption sites. Nevertheless, the adsorption of Pb(II) ions became slower as the number of active adsorption sites on the adsorbent surface decreased. The reason may be the slow diffusion of Pb(II) ions from surface sites into micropores or mesopores. As a result, lead adsorption has occurred not only on the surface but also in the pores of nanocomposite. Previous studies have reported similar results [84,85]. Metal ions have been reported to easily form poly-nuclear species and hydrolysis due to the smaller value of their hydrolysis constant. Consequently, the adsorbents adsorb these metal ions more defectively than free metal ions [86]. Upon reaching equilibrium, the absorption of Pb(II) ions slows down considerably. Accordingly, based on these findings, a contact time of 250, 420, and 700 min for the Pb(II) adsorption was selected in the subsequent isotherm studies, using RS, RSAC, and nZVFe–RSAC, respectively.

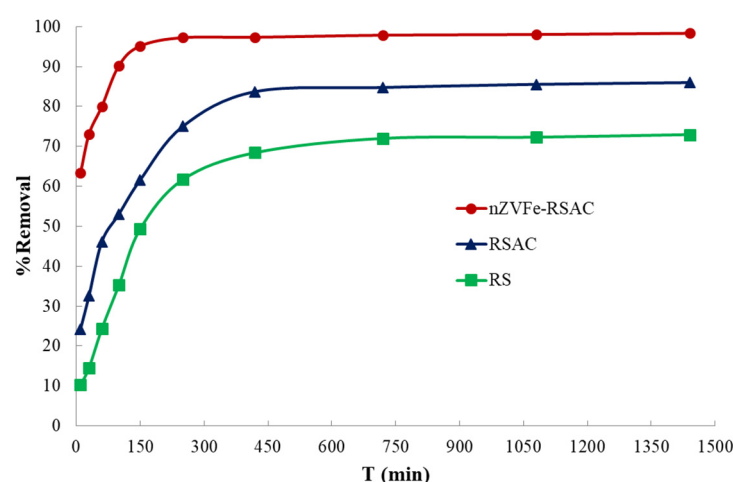


Figure 7. Effect of the exposure time on the Pb(II) adsorption by RS, RSAC, and nZVFe–RSAC ($C_0 = 100 \text{ mg L}^{-1}$; $T = 25 \text{ }^\circ\text{C}$).

A number of well-established and widely accepted models were applied to the experimental data in order to gain a more detailed understanding of the adsorption process from Pb(II) to adsorbents. Table 4 illustrates the kinetic parameters for the adsorption of Pb(II) on the RS, RSAC, and nZVFe–RSAC. Figure 8 also illustrates the fit of kinetic models to Pb(II) adsorption by RS, RSAC, and nZVFe–RSAC. Generally speaking, the adsorption of Pb(II) ions on the nZVFe–RSAC is associated with a pseudo-second-order kinetic model (Table 4 and Figure 8), suggesting that the adsorption is associated with the diffusion of Pb(II) ions within the porous structure of the nanocomposite [87]. Additionally, as shown in Table 4, nZVFe–RSAC had the highest initial adsorption rate ($h = 3.57$), which proves that the nanocomposite reacts with Pb(II) ions much faster than other adsorbents under similar conditions.

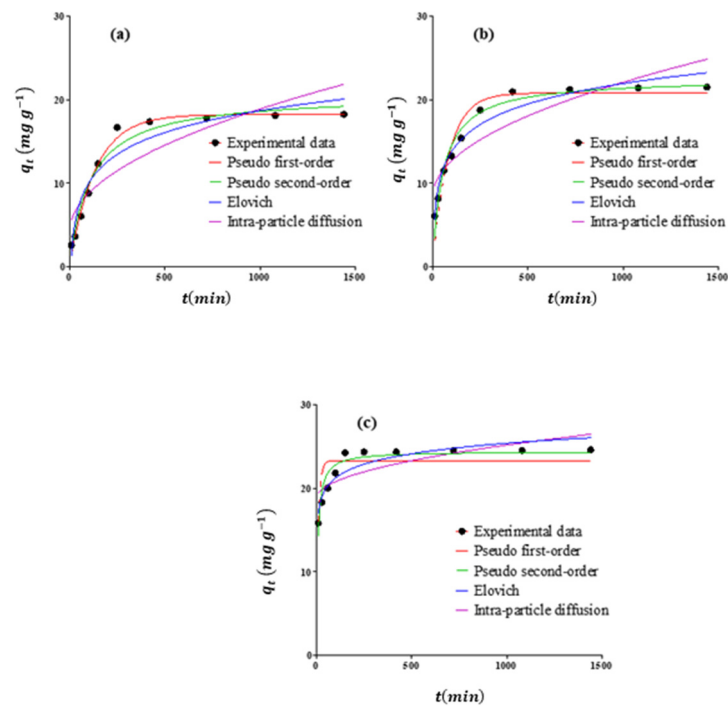


Figure 8. Pb(II) adsorption kinetics by (a) RS, (b) RSAC, and (c) nZVFe-RSAC.

3.5. Initial Concentration of Lead and Isotherm Study

Various Pb(II) concentrations were evaluated to determine how they affect the adsorption process (from 10 to 1000 mg L⁻¹). Based on Figure 9, it is evident that all the adsorbents exhibit an initial increase in Pb(II) adsorption capacity with an increase in Pb(II) concentration but then fail to demonstrate any significant change in Pb(II) adsorption capacity. Due to increased interaction between Pb(II) ions and adsorbents, the Pb(II) adsorption uptake increases with the increasing initial Pb(II) concentration. In higher concentrations of metal ions, fewer binding sites are available on the surface of the adsorbent, resulting in a decrease in the efficiency of removal. This has resulted in a saturation of the active sites on the adsorbent, indicating that less desirable sites were involved in the adsorption process [84]. The nZVFe-RSAC nanocomposite had 99.8% and 60.0% removal efficiencies at initial Pb(II) concentrations of 10 and 1000 mg L⁻¹, respectively. The maximum adsorption capacities of the RS, RSAC, and the nZVFe-RSAC for Pb(II) were 22.4, 58.3, and 120.0 (mg g⁻¹), respectively (Figure 9).

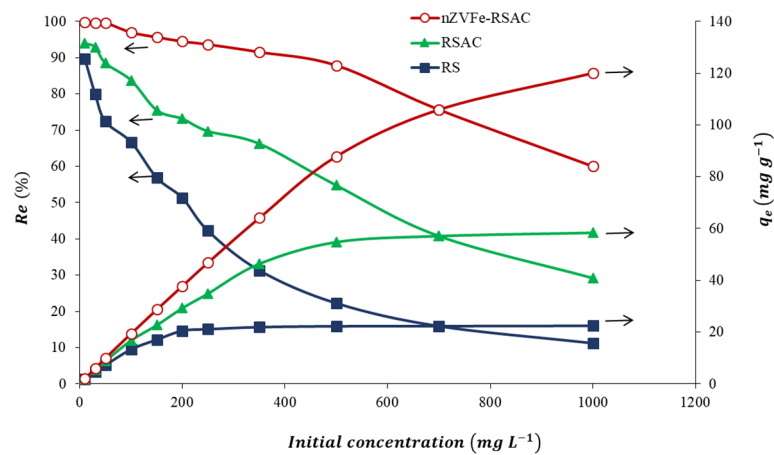


Figure 9. Effect of the initial Pb(II) concentration on the adsorption capacities of RS, RSAC, and nZVFe-RSAC (sorbent dosage = 6 (g L⁻¹), T = 25 °C).

Pb(II) adsorption processes by adsorbents were modeled by using the Redlich–Peterson, Langmuir–Freundlich, Freundlich, and Langmuir isotherms. A determination coefficient (R^2) was used to evaluate the fit of the data to the model. Figure 10 illustrates the application of isotherm models to experimental results. Furthermore, Table 5 provides information regarding the model parameters, R^2 , and SEE values for the adsorption of Pb(II) by adsorbents. In the case of the nZVFe–RSAC, the experimental adsorption data agreed well with the Redlich–Peterson, Langmuir–Freundlich, Freundlich, and Langmuir isotherms models, but the Langmuir–Freundlich model ($R^2 = 0.996$) was more consistent (Table 5). Several scholars have demonstrated the validity of the Langmuir–Freundlich model for Pb(II) adsorption experimentally [36,88]. In Table 5, all calculated R_L values were within the range of 0 and 1.0, indicating an optimal adsorption [84]. As many factors play a role in solid–liquid systems, such as hydration forces, mass transfer, etc., it is more difficult to define equilibrium behavior in a sorption system, and conformity to a single isotherm does not reflect the entire process of adsorption. It is possible to describe liquid–solid adsorption data using both Langmuir and Freundlich isotherms at specific concentration ranges. According to the Langmuir–Freundlich isotherm model, multilayer adsorption can occur on heterogeneous surfaces. In these surfaces, there are spaces with different forces, where the molecules of the adsorbate bind [36,70]. As a result, it can be concluded that the lead adsorption by nZVFe–RSAC occurred on heterogeneous surfaces and was superficial and multilayered.

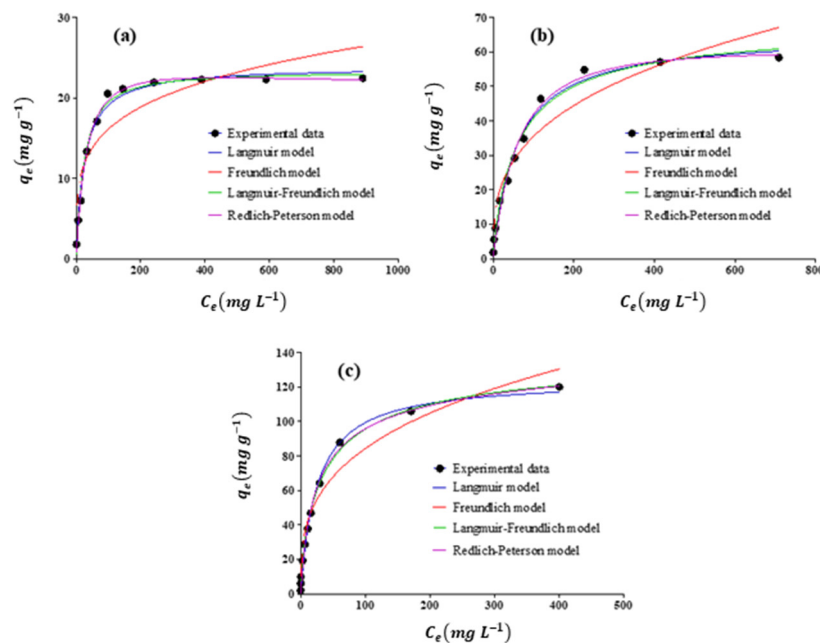


Figure 10. Adsorption isotherm plots for the removal of Pb(II) by (a) RS, (b) RSAC, and (c) nZVFe–RSAC.

Table 5. Adsorption Parameters of Langmuir, Freundlich, Langmuir–Freundlich, and Redlich–Peterson models for Pb(II) adsorption on varied adsorbents.

Model	Parameters	Adsorbent		
		RS	RSAC	nZVFe–RSAC
Langmuir	q_m ($mg\ g^{-1}$)	23.87	65.04	124.4
	k_L ($l\ mg^{-1}$)	0.039	0.017	0.040
	R_L	0.027–0.959	0.033–0.966	0.38–0.989
	R^2	0.989	0.984	0.989
	SEE	0.17	0.29	0.20

Table 5. Cont.

Model	Parameters	Adsorbent		
		RS	RSAC	nZVFe-RSAC
Freundlich	k_F (mg g^{-1})	5.70	7.91	19.79
	n	4.432	3.071	3.178
	R^2	0.832	0.928	0.964
	SEE	0.60	0.49	0.36
Langmuir-Freundlich	k_{LF} (l mg^{-1})	0.026	0.024	0.065
	q_m (mg g^{-1})	23.27	67.83	140.8
	n	0.874	1.118	1.322
	R^2	0.995	0.987	0.996
	SEE	0.03	0.24	0.05
Redlich-Peterson	a	0.759	0.990	6.14
	b	0.021	0.010	0.078
	g	1.068	1.059	0.921
	R^2	0.991	0.981	0.985
	SEE	0.05	0.31	0.27

3.6. Effect of Temperature and Thermodynamic Study

The thermodynamic experiments were carried out at four temperatures, namely 298, 308, 318, and 328 °K, separately (25–55 °C). Figure 11 shows the effect of adsorption temperature on the adsorption capacities and removal efficiencies of Pb(II) ions ($C_0 = 200 \text{ mg L}^{-1}$, pH = 6) by Rs, RSAC, and nZVFe-RSAC. It can be seen from Figure 11 that the Pb(II) adsorption capacities in the solution increased as the system temperature increased, rising from 37.59 (25 °C) to 39.58 mg g^{-1} (55 °C) for nZVFe-RSAC. As a result, in the case of nZVFe-RSAC, the removal efficiency of Pb(II) increased slightly from 93.96 (25 °C) to 98.94% (55 °C). In other words, high temperatures enable Pb(II) ions to diffuse into active adsorption sites of adsorbents, facilitating their adsorption [89].

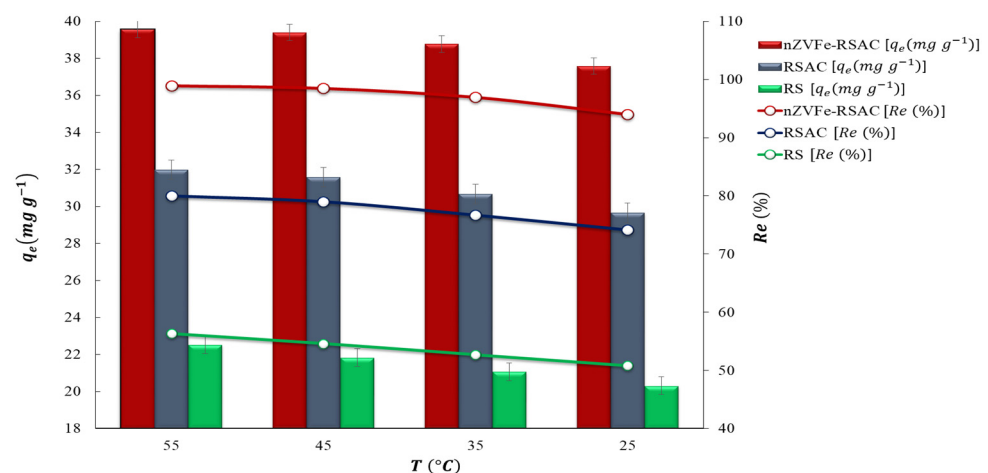


Figure 11. Effect of temperature on the adsorption of Pb(II) onto RS, RSAC, and nZVFe-RSAC (at 25, 35, 45, and 50 °C) ($C_0 = 200 \text{ mg L}^{-1}$).

In Table 6, the Gibbs free energy (ΔG^0), entropy (ΔS^0) and enthalpy (ΔH^0), values are presented. Negative values for ΔG^0 occurred when Pb(II) ions were adsorbed by nZVFe-RSAC at all tested temperature levels, indicating the adsorption process of Pb(II) onto the nanocomposite was a thermodynamically feasible and spontaneous process. The spontaneous nature of Pb(II) adsorption in our research is similar to that observed by [89]. Using the slope and intercept values from Figure 12’s linear regression analysis, the enthalpy and entropy parameters were calculated. In addition, the enthalpy value can

be used to determine the nature of the adsorption process, where a positive value indicates an endothermic process. Furthermore, adsorption is considered in the random-growth process when entropy is positive. In general, higher temperatures result in enhanced Pb(II) adsorption. The findings of this study are consistent with those of Patil et al. (2022) [90] and Senol-Arslan (2022) [91].

Table 6. Thermodynamics parameters for the adsorption of Pb(II) on nZVFe–RSAC nanocomposite.

Thermodynamic Parameters Adsorbent	T (°K)	ΔH^0 (kJ mol^{-1})	ΔS^0 ($\text{J mol}^{-1} \text{K}^{-1}$)	ΔG^0 (kJ mol^{-1})
RS	328	6.03	108.86	−29.70
	318			−28.61
	308			−27.51
	298			−26.43
RSAC	328	9.21	128.135	−32.78
	318			−31.62
	308			−30.29
	298			−28.96
nZVFe–RSAC	328	49.72	278.34	−41.38
	318			−39.16
	308			−36.09
	298			−33.16

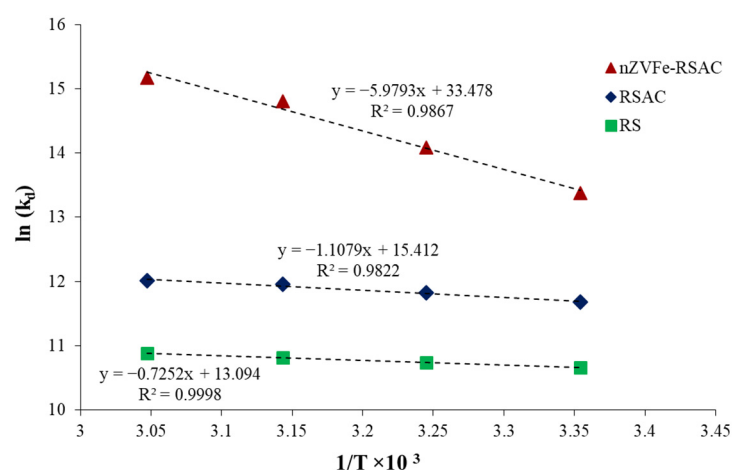


Figure 12. Temperature effect on sorption coefficients (k_d) for Pb(II) adsorption by RS, RSAC, and nZVFe–RSAC.

3.7. Effect of Competing Ions

A high level of selectivity for target pollutant adsorption is essential for the optimum use of an adsorbent. This is because surface water or groundwater or industrial effluent may also contain naturally competing ions. Figure 13 illustrates how competing ions affect nZVFe–RSAC lead-removal efficiency (Re %) at various concentrations of competing ions. According to Figure 13, the lead-removal efficiency in the presence of Cd(II) is not much affected, but Ni(II) has caused a decrease in lead removal to some extents. The effect of Cu(II) and Hg(II) on reducing lead absorption is far greater. So, at a concentration of 200 mg L^{-1} , the presence of Hg(II) caused a 55% reduction in lead removal efficiency. As discussed earlier, the removal of Pb(II) from the solution by the nZVFe–RSAC takes place through the redox process (Equation (15)). The standard reduction potential of this reaction is -0.44 V , which is lower than the standard reduction potential of many metals, such as Hg, Cd, Ni, Cu, and Pb [92]. The reduction reaction is highly feasible since it involves the conversion of high-valence metal ions into low-valence metal ions, thereby reducing their

solubility, toxicity, and carcinogenic properties [93,94]. Therefore, Fe^0 NPs can reduce any type of pollutant with a standard reduction potential higher than -0.44 V.

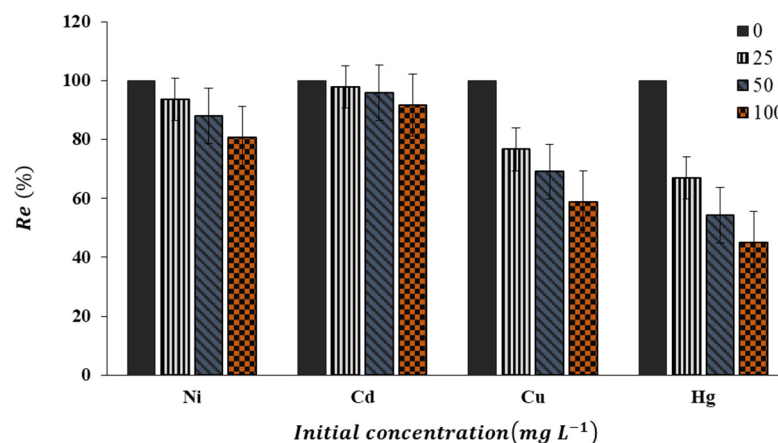


Figure 13. Effect of competing ions on Pb(II) removal efficiency by nZVFe-RSAC.

Pb(II) and Cd(II) have standard reduction potentials of -0.13 and -0.4 V, respectively. The standard potential of Hg(II), Cu(II), and Ni(II) are $+0.79$, $+0.34$, and -0.25 V, respectively. The standard reduction potential of Hg(II) and Cu(II) is more than the standard reduction potential of Pb^{2+} , and this issue has caused a great impact on the Pb(II) removal efficiency by nZVFe-RSAC. The standard reduction potential of Ni(II) is somewhat higher than that of Pb(II), and to some extent, Ni(II) in the competition has caused the lead-removal efficiency to decrease. Therefore, the effect of the presence of competing ions on reducing the Pb(II)-removal efficiency by the nZVFe-RSAC can be stated as follows: $\text{Hg} > \text{Cu} > \text{Ni} > \text{Cd}$.

3.8. Recyclability and Reuse of nZVFe-RSAC

A series of relevant experiments was conducted in order to assess the recyclability of nZVFe-RSAC (Figure 14). Following six consecutive recycling cycles, the removal efficiency of Pb(II) decreased from 99.6 to 43.4%. This could be attributed to the exhaustion of nZVFe particles due to chemical reduction and the incomplete resolution of precipitated and absorbed ions [17,25,95]. The nZVFe-RSAC achieved a 65% removal efficiency of Pb(II) in the fifth consecutive recycle, indicating that, even after five cycles of recovery, this nanocomposite can achieve more than 60% of its initial removal efficiency.

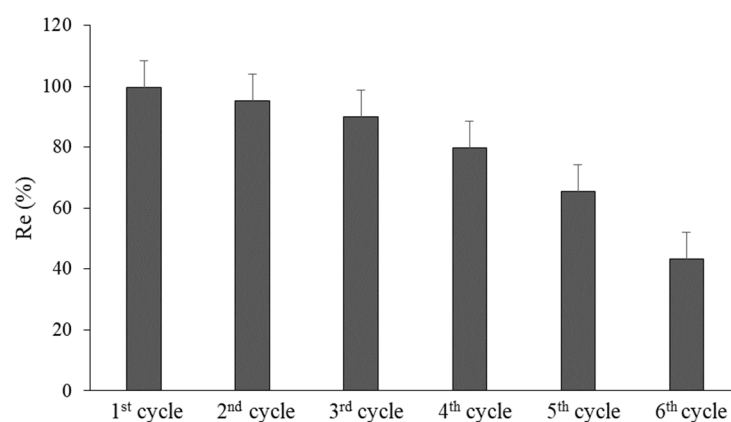


Figure 14. Pb(II) removal efficiency by nZVFe-RSAC after six consecutive cycles.

4. Conclusions

Wastewater treatment is a matter of concern, primarily because of the complexity, efficiency, and costs associated with this process [96–98]. In this context, zero-valent iron NPs provide a possible solution to the problem of water treatment. However, a strong

inclination to agglomerate has been reported as one of their significant drawbacks. To overcome this problem, the immobilization of nZVFe particles on porous host materials can be useful. In this study, with the aim of win-win cooperation, biomass-derived activated carbon and nZVFe particles were used to confirm the constructive interaction between the two counterparts and improve their respective remediation capabilities. In the first step, biomass-derived activated carbon was prepared from rice straw, using a thermal–chemical procedure (RSAC). Then the RSAC-supported nZVFe composite (nZVFe–RSAC) was synthesized by the sodium borohydride reduction method, and it was subsequently used to remove Pb(II) from the aqueous solution. Characterization by SEM and XRD techniques confirmed the high dispersion and activity of ZVFe nanoparticles with an average size of 46 nm after fixation on RSAC. Then this innovative nanocomposite was utilized to remove Pb(II) ions from the aqueous solution. In batch studies, the effects of various influencing factors on the process of Pb absorption, including contact time, amount of adsorbent, pH, temperature, and the initial concentration of the target pollutant, were investigated. The results showed that 6 (g L⁻¹) nZVFe–RSAC effectively removed about 97% of Pb(II) ions at pH = 6. Our investigation of the adsorption kinetics of Pb(II) ions on nZVFe–RSAC showed that this process follows a pseudo-second-order model. It strongly suggests that chemisorption, through the exchange or sharing of electrons between nanocomposite and Pb(II) ions, is the rate-limiting step in the adsorption process. Adsorption isotherm studies showed that the adsorption of Pb(II) onto nZVFe–RSAC fitted well with the Langmuir–Freundlich model ($R^2 = 0.996$), and the maximum absorption capacity of the nanocomposite was 140.8 (mg g⁻¹). Lastly, an investigation of the adsorption mechanism showed that nZVFe was involved in Pb(II) ions' removal through two main processes: (I) Pb(II) adsorption on the surface of nZVFe particles and (II) participation in the redox reaction directly. Subsequently, all intermediates produced through the redox reaction between iron nanoparticles and Pb(II) were adsorbed on the nZVFe–RSAC surface and did not enter the solution. In summary, the nZVFe–RSAC nanocomposite had a bright application prospect of good efficiency in immobilizing ZVFe nanoparticles, as well as a practical removal effect on Pb(II). It is necessary to conduct further research in order to determine whether different methods of preparing biomass-derived activated carbon result in improved nZVFe–RSAC nanocomposite characteristics and the ability to remove Pb(II), and also to determine the adsorption isotherm, kinetics, and thermodynamics in order to facilitate comparisons with other adsorbents.

Author Contributions: Conceptualization, S.S. and E.K.; methodology, S.S., E.K., S.A. and B.A.L.; investigation, S.S., E.K., S.A., V.D.R., T.M. and B.A.L.; writing—original draft preparation, S.S., E.K., S.A. and B.A.L.; writing—review and editing, S.S., E.K., S.A., V.D.R., T.M. and B.A.L. All authors have read and agreed to the published version of the manuscript.

Funding: This research received no external funding.

Institutional Review Board Statement: Not applicable.

Informed Consent Statement: Not applicable.

Data Availability Statement: All data, tables, figures, and results in the paper are our own and original.

Acknowledgments: V.D.R. and T.M. acknowledge support from the laboratory «Soil Health» of the Southern Federal University with the financial support of the Ministry of Science and Higher Education of the Russian Federation, agreement No. 075-15-2022-1122.

Conflicts of Interest: The authors declare that they have no conflict of interest.

References

1. Liu, W.; Zheng, J.; Ou, X.; Liu, X.; Song, Y.; Tian, C.; Rong, W.; Shi, Z.; Dang, Z.; Lin, Z. Effective extraction of Cr (VI) from hazardous gypsum sludge via controlling the phase transformation and chromium species. *Environ. Sci. Technol.* **2018**, *52*, 13336–13342. [[CrossRef](#)] [[PubMed](#)]
2. Lajayer, B.A.; Najafi, N.; Moghiseh, E.; Mosaferi, M.; Hadian, J. Micronutrient and heavy metal concentrations in basil plant cultivated on irradiated and non-irradiated sewage sludge-treated soil and evaluation of human health risk. *Regul. Toxicol. Pharmacol.* **2019**, *104*, 141–150. [[CrossRef](#)] [[PubMed](#)]
3. Shahi Khalaf Ansar, B.; Kavusi, E.; Dehghanian, Z.; Pandey, J.; Asgari Lajayer, B.; Price, G.W.; Astatkie, T. Removal of organic and inorganic contaminants from the air, soil, and water by algae. *Environ. Sci. Pollut. Res.* **2022**, 1–29. [[CrossRef](#)]
4. Nobaharan, K.; Abtahi, A.; Asgari Lajayer, B.; van Hullebusch, E.D. Effects of biochar dose on cadmium accumulation in spinach and its fractionation in a calcareous soil. *Arab. J. Geosci.* **2022**, *15*, 336. [[CrossRef](#)]
5. Chanthapon, N.; Sarkar, S.; Kidkhunthod, P.; Padungthon, S. Lead removal by a reusable gel cation exchange resin containing nano-scale zero valent iron. *Chem. Eng. J.* **2018**, *331*, 545–555. [[CrossRef](#)]
6. Lajayer, B.A.; Ghorbanpour, M.; Nikabadi, S. Heavy metals in contaminated environment: Destiny of secondary metabolite biosynthesis, oxidative status and phytoextraction in medicinal plants. *Ecotoxicol. Environ. Saf.* **2017**, *145*, 377–390. [[CrossRef](#)] [[PubMed](#)]
7. Asgari Lajayer, B.; Khadem Moghadam, N.; Maghsoodi, M.R.; Ghorbanpour, M.; Kariman, K. Phytoextraction of heavy metals from contaminated soil, water and atmosphere using ornamental plants: Mechanisms and efficiency improvement strategies. *Environ. Sci. Pollut. Res.* **2019**, *26*, 8468–8484. [[CrossRef](#)] [[PubMed](#)]
8. Pei, K.; Liu, T. Enhanced Cr (VI) removal with Pb (II) presence by Fe²⁺-activated persulfate and zero-valent iron system. *Environ. Technol.* **2022**, 1–15. [[CrossRef](#)]
9. Mandal, S.; Calderon, J.; Marpu, S.B.; Omary, M.A.; Shi, S.Q. Mesoporous activated carbon as a green adsorbent for the removal of heavy metals and Congo red: Characterization, adsorption kinetics, and isotherm studies. *J. Contam. Hydrol.* **2021**, *243*, 103869. [[CrossRef](#)]
10. Ren, J.; Zheng, L.; Su, Y.; Meng, P.; Zhou, Q.; Zeng, H.; Zhang, T.; Yu, H. Competitive adsorption of Cd (II), Pb (II) and Cu (II) ions from acid mine drainage with zero-valent iron/phosphoric titanium dioxide: XPS qualitative analyses and DFT quantitative calculations. *Chem. Eng. J.* **2022**, *445*, 136778. [[CrossRef](#)]
11. Asgari Lajayer, B.; Najafi, N.; Moghiseh, E.; Mosaferi, M.; Hadian, J. Removal of heavy metals (Cu²⁺ and Cd²⁺) from effluent using gamma irradiation, titanium dioxide nanoparticles and methanol. *J. Nanostructure Chem.* **2018**, *8*, 483–496. [[CrossRef](#)]
12. Heidarpour, A.; Aliasgharzad, N.; Khoshmanzar, E.; Lajayer, B.A. Bio-removal of Zn from contaminated water by using green algae isolates. *Environ. Technol. Innov.* **2019**, *16*, 100464. [[CrossRef](#)]
13. Wang, Z.; Liu, X.; Ni, S.-Q.; Zhuang, X.; Lee, T. Nano zero-valent iron improves anammox activity by promoting the activity of quorum sensing system. *Water Res.* **2021**, *202*, 117491. [[CrossRef](#)] [[PubMed](#)]
14. Danila, V.; Kumpiene, J.; Kasiuliene, A.; Vasarevičius, S. Immobilisation of metal (loid) s in two contaminated soils using micro and nano zerovalent iron particles: Evaluating the long-term stability. *Chemosphere* **2020**, *248*, 126054. [[CrossRef](#)]
15. Fajardo, C.; Martín, M.; Nande, M.; Botias, P.; García-Cantalejo, J.; Mengs, G.; Costa, G. Ecotoxicogenomic analysis of stress induced on *Caenorhabditis elegans* in heavy metal contaminated soil after nZVI treatment. *Chemosphere* **2020**, *254*, 126909. [[CrossRef](#)] [[PubMed](#)]
16. Zou, Y.; Wang, X.; Khan, A.; Wang, P.; Liu, Y.; Alsaedi, A.; Hayat, T.; Wang, X. Environmental remediation and application of nanoscale zero-valent iron and its composites for the removal of heavy metal ions: A review. *Environ. Sci. Technol.* **2016**, *50*, 7290–7304. [[CrossRef](#)]
17. Mortazavian, S.; An, H.; Chun, D.; Moon, J. Activated carbon impregnated by zero-valent iron nanoparticles (AC/nZVI) optimized for simultaneous adsorption and reduction of aqueous hexavalent chromium: Material characterizations and kinetic studies. *Chem. Eng. J.* **2018**, *353*, 781–795. [[CrossRef](#)]
18. Li, Y.; Cheng, W.; Sheng, G.; Li, J.; Dong, H.; Chen, Y.; Zhu, L. Synergetic effect of a pillared bentonite support on SE (VI) removal by nanoscale zero valent iron. *Appl. Catal. B Environ.* **2015**, *174*, 329–335. [[CrossRef](#)]
19. Liu, M.; Wang, Y.; Chen, L.; Zhang, Y.; Lin, Z. Mg (OH) 2 supported nanoscale zero valent iron enhancing the removal of Pb (II) from aqueous solution. *ACS Appl. Mater. Interfaces* **2015**, *7*, 7961–7969. [[CrossRef](#)]
20. Liu, T.; Wang, Z.-L.; Yan, X.; Zhang, B. Removal of mercury (II) and chromium (VI) from wastewater using a new and effective composite: Pumice-supported nanoscale zero-valent iron. *Chem. Eng. J.* **2014**, *245*, 34–40. [[CrossRef](#)]
21. Habish, A.J.; Lazarević, S.; Janković-Častvan, I.; Jokić, B.; Kovač, J.; Rogan, J.; Janačković, Đ.; Petrović, R. Nanoscale zerovalent iron (nZVI) supported by natural and acid-activated sepiolites: The effect of the nZVI/support ratio on the composite properties and Cd²⁺ adsorption. *Environ. Sci. Pollut. Res.* **2017**, *24*, 628–643. [[CrossRef](#)] [[PubMed](#)]
22. Fu, R.; Yang, Y.; Xu, Z.; Zhang, X.; Guo, X.; Bi, D. The removal of chromium (VI) and lead (II) from groundwater using sepiolite-supported nanoscale zero-valent iron (S-NZVI). *Chemosphere* **2015**, *138*, 726–734. [[CrossRef](#)] [[PubMed](#)]
23. Wang, C.; Xu, Z.; Ding, G.; Wang, X.; Zhao, M.; Ho, S.S.H.; Li, Y. Comprehensive study on the removal of chromate from aqueous solution by synthesized kaolin supported nanoscale zero-valent iron. *Desalin. Water Treat.* **2016**, *57*, 5065–5078. [[CrossRef](#)]

24. Bhowmick, S.; Chakraborty, S.; Mondal, P.; Van Renterghem, W.; Van den Berghe, S.; Roman-Ross, G.; Chatterjee, D.; Iglesias, M. Montmorillonite-supported nanoscale zero-valent iron for removal of arsenic from aqueous solution: Kinetics and mechanism. *Chem. Eng. J.* **2014**, *243*, 14–23. [[CrossRef](#)]
25. Wang, Z.; Chen, G.; Wang, X.; Li, S.; Liu, Y.; Yang, G. Removal of hexavalent chromium by bentonite supported organosolv lignin-stabilized zero-valent iron nanoparticles from wastewater. *J. Clean. Prod.* **2020**, *267*, 122009. [[CrossRef](#)]
26. Diao, Z.-H.; Xu, X.-R.; Chen, H.; Jiang, D.; Yang, Y.-X.; Kong, L.-J.; Sun, Y.-X.; Hu, Y.-X.; Hao, Q.-W.; Liu, L. Simultaneous removal of Cr (VI) and phenol by persulfate activated with bentonite-supported nanoscale zero-valent iron: Reactivity and mechanism. *J. Hazard. Mater.* **2016**, *316*, 186–193. [[CrossRef](#)] [[PubMed](#)]
27. Diao, Z.-H.; Xu, X.-R.; Jiang, D.; Kong, L.-J.; Sun, Y.-X.; Hu, Y.-X.; Hao, Q.-W.; Chen, H. Bentonite-supported nanoscale zero-valent iron/persulfate system for the simultaneous removal of Cr (VI) and phenol from aqueous solutions. *Chem. Eng. J.* **2016**, *302*, 213–222. [[CrossRef](#)]
28. Kong, X.; Han, Z.; Zhang, W.; Song, L.; Li, H. Synthesis of zeolite-supported microscale zero-valent iron for the removal of Cr⁶⁺ and Cd²⁺ from aqueous solution. *J. Environ. Manag.* **2016**, *169*, 84–90. [[CrossRef](#)]
29. Kim, S.A.; Kamala-Kannan, S.; Lee, K.-J.; Park, Y.-J.; Shea, P.J.; Lee, W.-H.; Kim, H.-M.; Oh, B.-T. Removal of Pb (II) from aqueous solution by a zeolite–nanoscale zero-valent iron composite. *Chem. Eng. J.* **2013**, *217*, 54–60. [[CrossRef](#)]
30. Sepehri, S.; Heidarpour, M.; Abedi-Koupai, J. Nitrate removal from aqueous solution using natural zeolite-supported zero-valent iron nanoparticles. *Soil Water Res.* **2014**, *9*, 224–232. [[CrossRef](#)]
31. Su, H.; Fang, Z.; Tsang, P.E.; Zheng, L.; Cheng, W.; Fang, J.; Zhao, D. Remediation of hexavalent chromium contaminated soil by biochar-supported zero-valent iron nanoparticles. *J. Hazard. Mater.* **2016**, *318*, 533–540. [[CrossRef](#)]
32. Liu, Z.; Zhang, F.; Hoekman, S.K.; Liu, T.; Gai, C.; Peng, N. Homogeneously dispersed zerovalent iron nanoparticles supported on hydrochar-derived porous carbon: Simple, in situ synthesis and use for dechlorination of PCBs. *ACS Sustain. Chem. Eng.* **2016**, *4*, 3261–3267. [[CrossRef](#)]
33. Liu, D.; Liu, Z.; Wang, C.; Lai, Y. Removal of uranium (VI) from aqueous solution using nanoscale zero-valent iron supported on activated charcoal. *J. Radioanal. Nucl. Chem.* **2016**, *310*, 1131–1137. [[CrossRef](#)]
34. Sepehri, S.; Nakhjavanimoghaddam, M. Batch removal of aqueous nitrate ions using an effective nano-biocomposite. *Glob. Nest J.* **2019**, *21*, 265–275. [[CrossRef](#)]
35. Arshadi, M.; Abdolmaleki, M.; Mousavinia, F.; Foroughifard, S.; Karimzadeh, A. Nano modification of NZVI with an aquatic plant *Azolla filiculoides* to remove Pb (II) and Hg (II) from water: Aging time and mechanism study. *J. Colloid Interface Sci.* **2017**, *486*, 296–308. [[CrossRef](#)] [[PubMed](#)]
36. Vázquez-Guerrero, A.; Cortés-Martínez, R.; Alfaro-Cuevas-Villanueva, R.; Rivera-Muñoz, E.M.; Huirache-Acuña, R. Cd (II) and Pb (II) adsorption using a composite obtained from moringa oleifera lam. Cellulose nanofibrils impregnated with iron nanoparticles. *Water* **2021**, *13*, 89. [[CrossRef](#)]
37. Yang, F.; He, Y.; Sun, S.; Chang, Y.; Zha, F.; Lei, Z. Walnut shell supported nanoscale Fe⁰ for the removal of Cu (II) and Ni (II) ions from water. *J. Appl. Polym. Sci.* **2016**, *133*, 43304–43309. [[CrossRef](#)]
38. Lee, C.-S.; Gong, J.; Huong, C.V.; Oh, D.-S.; Chang, Y.-S. Macroporous alginate substrate-bound growth of Fe⁰ nanoparticles with high redox activities for nitrate removal from aqueous solutions. *Chem. Eng. J.* **2016**, *298*, 206–213. [[CrossRef](#)]
39. Huang, J.-F.; Li, Y.-T.; Wu, J.-H.; Cao, P.-Y.; Liu, Y.-L.; Jiang, G.-B. Floatable, macroporous structured alginate sphere supporting iron nanoparticles used for emergent Cr (VI) spill treatment. *Carbohydr. Polym.* **2016**, *146*, 115–122. [[CrossRef](#)]
40. Toli, A.; Chalastara, K.; Mystrioti, C.; Xenidis, A.; Papassiopi, N. Incorporation of zero valent iron nanoparticles in the matrix of cationic resin beads for the remediation of Cr (VI) contaminated waters. *Environ. Pollut.* **2016**, *214*, 419–429. [[CrossRef](#)]
41. Liu, F.; Shan, C.; Zhang, X.; Zhang, Y.; Zhang, W.; Pan, B. Enhanced removal of EDTA-chelated Cu (II) by polymeric anion-exchanger supported nanoscale zero-valent iron. *J. Hazard. Mater.* **2017**, *321*, 290–298. [[CrossRef](#)] [[PubMed](#)]
42. Wang, X.; Zhang, S.; Li, J.; Xu, J.; Wang, X. Fabrication of Fe/Fe₃C@ porous carbon sheets from biomass and their application for simultaneous reduction and adsorption of uranium (VI) from solution. *Inorg. Chem. Front.* **2014**, *1*, 641–648. [[CrossRef](#)]
43. Shi, J.; Yi, S.; Long, C.; Li, A. Effect of Fe loading quantity on reduction reactivity of nano zero-valent iron supported on chelating resin. *Front. Environ. Sci. Eng.* **2015**, *9*, 840–849. [[CrossRef](#)]
44. Hu, B.; Chen, G.; Jin, C.; Hu, J.; Huang, C.; Sheng, J.; Sheng, G.; Ma, J.; Huang, Y. Macroscopic and spectroscopic studies of the enhanced scavenging of Cr (VI) and Se (VI) from water by titanate nanotube anchored nanoscale zero-valent iron. *J. Hazard. Mater.* **2017**, *336*, 214–221. [[CrossRef](#)] [[PubMed](#)]
45. Yang, S.; Chen, C.; Chen, Y.; Li, J.; Wang, D.; Wang, X.; Hu, W. Competitive adsorption of Pb^{II}, Ni^{II}, and Sr^{II} ions on graphene oxides: A combined experimental and theoretical study. *ChemPlusChem* **2015**, *80*, 480–484. [[CrossRef](#)]
46. Sheng, G.; Hu, J.; Li, H.; Li, J.; Huang, Y. Enhanced sequestration of Cr (VI) by nanoscale zero-valent iron supported on layered double hydroxide by batch and XAFS study. *Chemosphere* **2016**, *148*, 227–232. [[CrossRef](#)]
47. Sheng, G.; Tang, Y.; Linghu, W.; Wang, L.; Li, J.; Li, H.; Wang, X.; Huang, Y. Enhanced immobilization of ReO₄[−] by nanoscale zerovalent iron supported on layered double hydroxide via an advanced XAFS approach: Implications for TcO₄[−] sequestration. *Appl. Catal. B Environ.* **2016**, *192*, 268–276. [[CrossRef](#)]
48. Gosu, V.; Gurjar, B.R.; Surampalli, R.Y.; Zhang, T.C. Treatment of pyridine-bearing wastewater by nano zero-valent iron supported on activated carbon derived from agricultural waste. *Desalin. Water Treat.* **2016**, *57*, 6250–6260. [[CrossRef](#)]

49. Busch, J.; Meißner, T.; Potthoff, A.; Bleyl, S.; Georgi, A.; Mackenzie, K.; Trabitzsch, R.; Werban, U.; Oswald, S.E. A field investigation on transport of carbon-supported nanoscale zero-valent iron (nZVI) in groundwater. *J. Contam. Hydrol.* **2015**, *181*, 59–68. [[CrossRef](#)]
50. Fan, M.; Li, T.; Hu, J.; Cao, R.; Wu, Q.; Wei, X.; Li, L.; Shi, X.; Ruan, W. Synthesis and characterization of reduced graphene oxide-supported nanoscale zero-valent iron (nZVI/rGO) composites used for Pb (II) removal. *Materials* **2016**, *9*, 687. [[CrossRef](#)]
51. Fan, H.; Ren, H.; Ma, X.; Zhou, S.; Huang, J.; Jiao, W.; Qi, G.; Liu, Y. High-gravity continuous preparation of chitosan-stabilized nanoscale zero-valent iron towards Cr (VI) removal. *Chem. Eng. J.* **2020**, *390*, 124639. [[CrossRef](#)]
52. Sheng, G.; Alsaedi, A.; Shammakh, W.; Monaque, S.; Sheng, J.; Wang, X.; Li, H.; Huang, Y. Enhanced sequestration of selenite in water by nanoscale zero valent iron immobilization on carbon nanotubes by a combined batch, XPS and XAFS investigation. *Carbon* **2016**, *99*, 123–130. [[CrossRef](#)]
53. Siciliano, A. Removal of Cr (VI) from water using a new reactive material: Magnesium Oxide supported nanoscale zero-valent iron. *Materials* **2016**, *9*, 666. [[CrossRef](#)] [[PubMed](#)]
54. Du, Q.; Li, G.; Zhang, S.; Song, J.; Yang, F. High-dispersion zero-valent iron particles stabilized by artificial humic acid for lead ion removal. *J. Hazard. Mater.* **2020**, *383*, 121170. [[CrossRef](#)]
55. Wang, X.; Liang, D.; Wang, Y.; Peijnenburg, W.J.; Monikh, F.A.; Zhao, X.; Dong, Z.; Fan, W. A critical review on the biological impact of natural organic matter on nanomaterials in the aquatic environment. *Carbon Res.* **2022**, *1*, 13. [[CrossRef](#)]
56. Yan, B.; Feng, L.; Zheng, J.; Zhang, Q.; Jiang, S.; Zhang, C.; Ding, Y.; Han, J.; Chen, W.; He, S. High performance supercapacitors based on wood-derived thick carbon electrodes synthesized via green activation process. *Inorg. Chem. Front.* **2022**, *9*, 6108–6123. [[CrossRef](#)]
57. Yan, B.; Zheng, J.; Feng, L.; Du, C.; Jian, S.; Yang, W.; Wu, Y.A.; Jiang, S.; He, S.; Chen, W. Wood-derived biochar as thick electrodes for high-rate performance supercapacitors. *Biochar* **2022**, *4*, 50. [[CrossRef](#)]
58. Obey, G.; Adelaide, M.; Ramaraj, R. Biochar derived from non-customized matamba fruit shell as an adsorbent for wastewater treatment. *J. Bioresour. Bioprod.* **2022**, *7*, 109–115. [[CrossRef](#)]
59. Liu, Z.; Xu, Z.; Xu, L.; Buyong, F.; Chay, T.C.; Li, Z.; Cai, Y.; Hu, B.; Zhu, Y.; Wang, X. Modified biochar: Synthesis and mechanism for removal of environmental heavy metals. *Carbon Res.* **2022**, *1*, 8. [[CrossRef](#)]
60. Awang, N.A.; Wan Salleh, W.N.; Aziz, F.; Yusof, N.; Ismail, A.F. A review on preparation, surface enhancement and adsorption mechanism of biochar-supported nano zero-valent iron adsorbent for hazardous heavy metals. *J. Chem. Technol. Biotechnol.* **2022**, *98*, 22–44. [[CrossRef](#)]
61. Ahmad, S.; Liu, X.; Tang, J.; Zhang, S. Biochar-supported nanosized zero-valent iron (nZVI/BC) composites for removal of nitro and chlorinated contaminants. *Chem. Eng. J.* **2021**, *431*, 133187. [[CrossRef](#)]
62. FAO. *FAOSTAT Statistical Database*; Food and Agriculture Organization of the United Nations: Rome, Italy, 2020.
63. Motlagh, E.K.; Asasian-Kolur, N.; Sharifian, S.; Pirbazari, A.E. Sustainable rice straw conversion into activated carbon and nano-silica using carbonization-extraction process. *Biomass Bioenergy* **2021**, *144*, 105917. [[CrossRef](#)]
64. Jiang, S.-F.; Ling, L.-L.; Chen, W.-J.; Liu, W.-J.; Li, D.-C.; Jiang, H. High efficient removal of bisphenol A in a peroxymonosulfate/iron functionalized biochar system: Mechanistic elucidation and quantification of the contributors. *Chem. Eng. J.* **2019**, *359*, 572–583. [[CrossRef](#)]
65. Ruiz-Torres, C.A.; Araujo-Martínez, R.F.; Martínez-Castañón, G.A.; Morales-Sánchez, J.E.; Guajardo-Pacheco, J.M.; González-Hernández, J.; Lee, T.-J.; Shin, H.-S.; Hwang, Y.; Ruiz, F. Preparation of air stable nanoscale zero valent iron functionalized by ethylene glycol without inert condition. *Chem. Eng. J.* **2018**, *336*, 112–122. [[CrossRef](#)]
66. Charoensook, K.; Huang, C.-L.; Tai, H.-C.; Lanjapalli, V.V.K.; Chiang, L.-M.; Hosseini, S.; Lin, Y.-T.; Li, Y.-Y. Preparation of porous nitrogen-doped activated carbon derived from rice straw for high-performance supercapacitor application. *J. Taiwan Inst. Chem. Eng.* **2021**, *120*, 246–256. [[CrossRef](#)]
67. Momčilović, M.; Purenović, M.; Bojić, A.; Zarubica, A.; Randelović, M. Removal of lead (II) ions from aqueous solutions by adsorption onto pine cone activated carbon. *Desalination* **2011**, *276*, 53–59. [[CrossRef](#)]
68. Üzümlü, Ç.; Shahwan, T.; Eroğlu, A.E.; Hallam, K.R.; Scott, T.B.; Lieberwirth, I. Synthesis and characterization of kaolinite-supported zero-valent iron nanoparticles and their application for the removal of aqueous Cu²⁺ and Co²⁺ ions. *Appl. Clay Sci.* **2009**, *43*, 172–181. [[CrossRef](#)]
69. Wu, H.-Y.; Chen, S.S.; Liao, W.; Wang, W.; Jang, M.-F.; Chen, W.-H.; Ahamad, T.; Alshehri, S.M.; Hou, C.-H.; Lin, K.-S. Assessment of agricultural waste-derived activated carbon in multiple applications. *Environ. Res.* **2020**, *191*, 110176. [[CrossRef](#)]
70. Rajahmundry, G.K.; Garlapati, C.; Kumar, P.S.; Alwi, R.S.; Vo, D.-V.N. Statistical analysis of adsorption isotherm models and its appropriate selection. *Chemosphere* **2021**, *276*, 130176. [[CrossRef](#)]
71. Menezes, J.M.C.; da Silva Bento, A.M.; da Silva, J.H.; de Paula Filho, F.J.; da Costa, J.G.M.; Coutinho, H.D.M.; Teixeira, R.N.P. Equilibrium, kinetics and thermodynamics of lead (II) adsorption in bioadsorbent composed by Caryocar coriaceum Wittm barks. *Chemosphere* **2020**, *261*, 128144. [[CrossRef](#)] [[PubMed](#)]
72. Pandey, S.; Fosso-Kankeu, E.; Spiro, M.; Waanders, F.; Kumar, N.; Ray, S.S.; Kim, J.; Kang, M. Equilibrium, kinetic, and thermodynamic studies of lead ion adsorption from mine wastewater onto MoS₂-clinoptilolite composite. *Mater. Today Chem.* **2020**, *18*, 100376. [[CrossRef](#)]
73. Qin, C.; Chen, Y.; Gao, J.-M. Manufacture and characterization of activated carbon from marigold straw (*Tagetes erecta* L.) by H₃PO₄ chemical activation. *Mater. Lett.* **2014**, *135*, 123–126. [[CrossRef](#)]

74. Bhattacharyya, P.; Bhaduri, D.; Adak, T.; Munda, S.; Satapathy, B.; Dash, P.; Padhy, S.; Pattanayak, A.; Routray, S.; Chakraborti, M. Characterization of rice straw from major cultivars for best alternative industrial uses to cutoff the menace of straw burning. *Ind. Crops Prod.* **2020**, *143*, 111919. [[CrossRef](#)]
75. Birks, L.; Friedman, H. Particle size determination from X-ray line broadening. *J. Appl. Phys.* **1946**, *17*, 687–692. [[CrossRef](#)]
76. Li, S.; Yang, F.; Zhang, Y.; Lan, Y.; Cheng, K. Performance of lead ion removal by the three-dimensional carbon foam supported nanoscale zero-valent iron composite. *J. Clean. Prod.* **2021**, *294*, 125350. [[CrossRef](#)]
77. Bae, S.; Collins, R.N.; Waite, T.D.; Hanna, K. Advances in surface passivation of nanoscale zerovalent iron: A critical review. *Environ. Sci. Technol.* **2018**, *52*, 12010–12025. [[CrossRef](#)]
78. Zhang, X.; Lin, S.; Lu, X.-Q.; Chen, Z.-I. Removal of Pb (II) from water using synthesized kaolin supported nanoscale zero-valent iron. *Chem. Eng. J.* **2010**, *163*, 243–248. [[CrossRef](#)]
79. Li, W.; Brunner, P.; Franssen, H.-J.H.; Li, Z.; Wang, Z.; Zhang, Z.; Wang, W. Potential evaporation dynamics over saturated bare soil and an open water surface. *J. Hydrol.* **2020**, *590*, 125140. [[CrossRef](#)]
80. Gao, C.; Wang, X.-L.; An, Q.-D.; Xiao, Z.-Y.; Zhai, S.-R. Synergistic preparation of modified alginate aerogel with melamine/chitosan for efficiently selective adsorption of lead ions. *Carbohydr. Polym.* **2021**, *256*, 117564. [[CrossRef](#)]
81. Zhang, W.-X. Nanoscale iron particles for environmental remediation: An overview. *J. Nanopart. Res.* **2003**, *5*, 323–332. [[CrossRef](#)]
82. Arshadi, M.; Soleymanzadeh, M.; Salvacion, J.; SalimiVahid, F. Nanoscale zero-valent iron (NZVI) supported on sineguas waste for Pb (II) removal from aqueous solution: Kinetics, thermodynamic and mechanism. *J. Colloid Interface Sci.* **2014**, *426*, 241–251. [[CrossRef](#)] [[PubMed](#)]
83. Wang, T.C.; Rubner, M.F.; Cohen, R.E. Polyelectrolyte multilayer nanoreactors for preparing silver nanoparticle composites: Controlling metal concentration and nanoparticle size. *Langmuir* **2002**, *18*, 3370–3375. [[CrossRef](#)]
84. Jalu, R.G.; Chamada, T.A.; Kasirajan, R. Calcium oxide nanoparticles synthesis from hen eggshells for removal of lead (Pb (II)) from aqueous solution. *Environ. Chall.* **2021**, *4*, 100193. [[CrossRef](#)]
85. Kavand, M.; Eslami, P.; Razeh, L. The adsorption of cadmium and lead ions from the synthesis wastewater with the activated carbon: Optimization of the single and binary systems. *J. Water Process Eng.* **2020**, *34*, 101151. [[CrossRef](#)]
86. Tabesh, S.; Davar, F.; Loghman-Estarki, M.R. Preparation of γ -Al₂O₃ nanoparticles using modified sol-gel method and its use for the adsorption of lead and cadmium ions. *J. Alloys Compd.* **2018**, *730*, 441–449. [[CrossRef](#)]
87. Hubbe, M.A.; Azizian, S.; Douven, S. Implications of apparent pseudo-second-order adsorption kinetics onto cellulosic materials: A review. *BioResources* **2019**, *14*, 7582–7626. [[CrossRef](#)]
88. Abo El-Reesh, G.Y.; Farghali, A.A.; Taha, M.; Mahmoud, R.K. Novel synthesis of Ni/Fe layered double hydroxides using urea and glycerol and their enhanced adsorption behavior for Cr (VI) removal. *Sci. Rep.* **2020**, *10*, 587. [[CrossRef](#)]
89. Alqadami, A.A.; Naushad, M.; ALOthman, Z.A.; Alsuhybani, M.; Algamdi, M. Excellent adsorptive performance of a new nanocomposite for removal of toxic Pb (II) from aqueous environment: Adsorption mechanism and modeling analysis. *J. Hazard. Mater.* **2020**, *389*, 121896. [[CrossRef](#)]
90. Patil, S.A.; Suryawanshi, U.P.; Harale, N.S.; Patil, S.K.; Vadiyar, M.M.; Luwang, M.N.; Anuse, M.A.; Kim, J.H.; Kolekar, S.S. Adsorption of toxic Pb (II) on activated carbon derived from agriculture waste (Mahogany fruit shell): Isotherm, kinetic and thermodynamic study. *Int. J. Environ. Anal. Chem.* **2020**, 1–17. [[CrossRef](#)]
91. Senol-Arslan, D. Isotherms, kinetics and thermodynamics of pb (ii) adsorption by crosslinked chitosan/sepiolite composite. *Polym. Bull.* **2022**, *79*, 3911–3928. [[CrossRef](#)]
92. Liang, W.; Wang, G.; Peng, C.; Tan, J.; Wan, J.; Sun, P.; Li, Q.; Ji, X.; Zhang, Q.; Wu, Y. Recent advances of carbon-based nano zero valent iron for heavy metals remediation in soil and water: A critical review. *J. Hazard. Mater.* **2022**, *426*, 127993. [[CrossRef](#)] [[PubMed](#)]
93. Fan, C.; Chen, N.; Qin, J.; Yang, Y.; Feng, C.; Li, M.; Gao, Y. Biochar stabilized nano zero-valent iron and its removal performance and mechanism of pentavalent vanadium (V (V)). *Colloids Surf. A Physicochem. Eng. Asp.* **2020**, *599*, 124882. [[CrossRef](#)]
94. Wang, W.; Hu, B.; Wang, C.; Liang, Z.; Cui, F.; Zhao, Z.; Yang, C. Cr (VI) removal by micron-scale iron-carbon composite induced by ball milling: The role of activated carbon. *Chem. Eng. J.* **2020**, *389*, 122633. [[CrossRef](#)]
95. Yang, F.; Zhang, S.; Sun, Y.; Cheng, K.; Li, J.; Tsang, D.C. Fabrication and characterization of hydrophilic corn stalk biochar-supported nanoscale zero-valent iron composites for efficient metal removal. *Bioresour. Technol.* **2018**, *265*, 490–497. [[CrossRef](#)] [[PubMed](#)]
96. Xu, D.; Li, J.; Liu, J.; Qu, X.; Ma, H. Advances in continuous flow aerobic granular sludge: A review. *Process Saf. Environ. Prot.* **2022**, *163*, 27–35. [[CrossRef](#)]
97. Nobaharan, K.; Bagheri Novair, S.; Asgari Lajayer, B.; van Hullebusch, E.D. Phosphorus removal from wastewater: The potential use of biochar and the key controlling factors. *Water* **2021**, *13*, 517. [[CrossRef](#)]
98. Guan, Q.; Zeng, G.; Song, J.; Liu, C.; Wang, Z.; Wu, S. Ultrasonic power combined with seed materials for recovery of phosphorus from swine wastewater via struvite crystallization process. *J. Environ. Manag.* **2021**, *293*, 112961. [[CrossRef](#)]

Disclaimer/Publisher's Note: The statements, opinions and data contained in all publications are solely those of the individual author(s) and contributor(s) and not of MDPI and/or the editor(s). MDPI and/or the editor(s) disclaim responsibility for any injury to people or property resulting from any ideas, methods, instructions or products referred to in the content.